Acta Materialia 98 (2015) 64–80

Contents lists available at ScienceDirect

Acta Materialia

journal homepage: www.elsevier.com/locate/actamat

# The competition between metastable and equilibrium S ($Al_2CuMg$) phase during the decomposition of Al—Cu—Mg alloys

M.J. Styles [a,*], R.K.W. Marceau [b], T.J. Bastow [a], H.E.A. Brand [c], M.A. Gibson [a,d], C.R. Hutchinson [d]

[a] CSIRO Manufacturing Flagship, Clayton, VIC 3168, Australia
[b] Institute for Frontier Materials, Deakin University, Geelong, VIC 3216, Australia
[c] Australian Synchrotron, Clayton, VIC 3168, Australia
[d] Department of Materials Science and Engineering, Monash University, Clayton, VIC 3800, Australia

ARTICLE INFO

*Article history:*
Received 14 April 2015
Accepted 3 July 2015
Available online 18 July 2015

*Keywords:*
Al—Cu—Mg
Precipitation
S phase
Powder diffraction
Rietveld refinement
Atom probe tomography

ABSTRACT

The decomposition sequence of the supersaturated solid solution leading to the formation of the equilibrium S ($Al_2CuMg$) phase in Al—Cu—Mg alloys has long been the subject of ambiguity and debate. Recent high-resolution synchrotron powder diffraction experiments have shown that the decomposition sequence does involve a metastable variant of the S phase (denoted S1), which has lattice parameters that are distinctly different to those of the equilibrium S phase (denoted S2). In this paper, the difference between these two phases is resolved using high-resolution synchrotron and neutron powder diffraction and atom probe tomography, and the transformation from S1 to S2 is characterised in detail by *in situ* synchrotron powder diffraction. The results of these experiments confirm that there are no significant differences between the crystal structures of S1 and S2, however, the powder diffraction and atom probe measurements both indicate that the S1 phase forms with a slight deficiency in Cu. The *in situ* isothermal aging experiments show that S1 forms rapidly, reaching its maximum concentration in only a few minutes at high temperatures, while complete conversion to the S2 phase can take thousands of hours at low temperature. The kinetics of S phase precipitation have been quantitatively analysed for the first time and it is shown that S1 phase forms with an average activation energy of 75 kJ/mol, which is much lower than the activation energy for Cu and Mg diffusion in an Al matrix (136 kJ/mol and 131 kJ/mol, respectively). The mechanism of the replacement of S1 with the equilibrium S2 phase is discussed.


## 1. Introduction

Al–Cu–Mg alloys are the basis of the important 2xxx series of age-hardenable aluminium alloys, which are widely used in applications where good specific strength is required. The properties of these alloys, including their yield strength, toughness and susceptibility to corrosion, are largely controlled by the distribution of secondary phase precipitates that are formed within the matrix phase during heat treatment. Alloys with Cu:Mg ratios of ~2:1 (in wt.%) lie in the ($\alpha$ + S) two-phase field of the ternary phase diagram, where $\alpha$ is the fcc Al matrix phase and S is the orthorhombic $Al_2CuMg$ phase first identified by Perlitz and Westgren [1]. Whilst the equilibrium state ($\alpha$ + S) is widely accepted, many other aspects of the decomposition of the supersaturated solid solution (SSSS) to the final equilibrium state continue to be the subject of ambiguity and debate. In particular, the existence of metastable variants of the S phase remain topics of considerable discussion [2–8].

The classic precipitation sequence first proposed by Bagaryatsky [9,10] (as summarised by Silcock [11]) for Al—Cu—Mg alloys in this composition region is:

$$\text{SSSS} \rightarrow \text{GPB zones} \rightarrow S'' + S' \rightarrow S' + S \rightarrow S$$

where GPB (Guinier–Preston–Bagaryatsky) zones are small, rod-like particles (1–2 nm in diameter) rich in Cu and Mg [11,12], and S″ and S′ refer to distorted, metastable S phase structures with different levels of coherence with the matrix [9,10]. According to the sequence proposed by Bagaryatsky, the next precipitate phase to form after the GPB zones is S″ (sometimes termed GPB2), which is reported to be entirely coherent with the matrix and has a plate like morphology [13–17]. However, it is noteworthy that several other investigations were unable to confirm the existence of this phase [11,18–21], and there is no agreed structure for S″ [22].

It is generally agreed, however, that the peak strength for Al—Cu—Mg alloys is achieved after further aging, when the GPB

* Corresponding author.
*E-mail address:* Mark.Styles@csiro.au (M.J. Styles).

http://dx.doi.org/10.1016/j.actamat.2015.07.011
1359-6454/

zones and S″ (if present) begin to transform into larger S′ and S phase precipitates [22]. In the classical definition proposed by Bagaryatsky, the S′ phase corresponds to elongated particles possessing a semi-coherent interface with the matrix, while the equilibrium S phase is thought to have a more incoherent interface [9–11]. In recent times the distinction between S′ and S has been questioned, with some authors arguing that the small difference in lattice parameters is insufficient to designate a new phase [2,23]. However, other reports have shown that the S phase can adopt a range of different morphologies and orientation relationships within the Al matrix [3–7], and that the properties of the bulk material in the peak and over aged states are dependent on the proportion of precipitates with coherent interfaces with the matrix [7]. Clearly the distinction between S phase precipitates with coherent/semi-coherent interfaces and incoherent interfaces, classically defined as S′ and S respectively, is a matter of significant technological interest.

Recent high-resolution synchrotron powder diffraction measurements made by the present authors on a series of Al—2.5Cu—1.5Mg (wt.%) samples isothermally aged for different times, have revealed compelling evidence that the precipitation sequence does involve the formation of a metastable variant of the S phase [8]. Specifically, two sets of S phase diffraction peaks were observed, the relative intensity of which varied systematically with aging time. These diffraction patterns were successfully modelled using two S phase structures, denoted S1 (metastable) and S2 (equilibrium), with lattice parameters that are consistently and significantly different. Examples of several key peaks corresponding to the S1 and S2 phases, from the work of Styles et al. [8] are shown in Fig. 1, illustrating the distinct difference between the S1 and S2 phases. The lattice parameters of S2 were found to be in excellent agreement with those refined by Heying et al. [24] for the equilibrium S phase, while the *a* lattice parameter of S1 is very close to that of the α phase matrix. The matching of the S1 *a* lattice parameter with that of α-Al provides an opportunity for this variant to exhibit some coherency (or semi-coherency) with the matrix, which is in good agreement with the classical definition of the S′ phase.

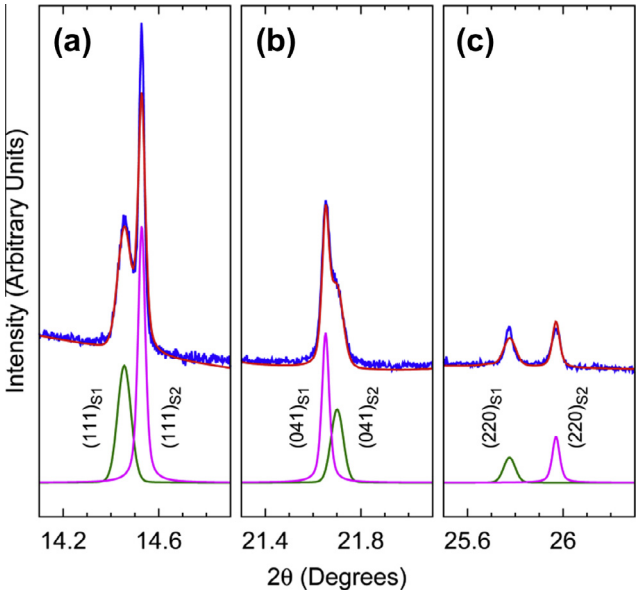


**Fig. 1.** Selected regions of the observed (blue) and calculated (red) diffraction patterns obtained (in the work of Styles et al. [8]) from a sample of Al—2.5Cu—1.5Mg (wt.%) aged at 350 °C for 10 h, highlighting the two sets of S phase peaks. The deconvoluted profiles of the (1 1 1), (0 4 1) and (2 2 0) peaks of the S1 (green) and S2 (pink) phases are shown. All three regions have been plotted on the same vertical scale. (For interpretation of the references to colour in this figure legend, the reader is referred to the web version of this article.)

Given that the lattice parameters of S1 are distinctly different from the equilibrium S2 phase, it is possible that an unknown structural modification may be responsible, such as the substitution of Al or vacancies onto different sites within the S1 crystal structure. Such modifications would be difficult to detect using TEM-based techniques, but should be amenable to chemical and crystallographic techniques such as atom probe tomography, X-ray and neutron diffraction. Alternatively, the difference in lattice parameters may be a result of the strain imparted by the matrix, and hence the kinetics of the transformation from S1 to S2 (and the corresponding evolution of the lattice parameters) may provide a valuable insight into the mechanism of the transformation.

The present investigation has two objectives. The first is to identify the structural features responsible for the difference between the S1 and S2 phases. One possibility is that Al atoms substitute onto the Mg site within the S1 crystal structure. A combination of high-resolution synchrotron X-ray and neutron powder diffraction has been used to investigate this, as Al-Mg substitution would be hard to detect using X-ray diffraction techniques alone due to the similar X-ray scattering factors of Al and Mg. In comparison, the neutron scattering lengths for Al and Mg are significantly different (3.449 and 5.375 fm, respectively), and the combination of the two techniques enables the site occupation factors of the two S phases to be refined. Changes in the composition of the S phases observed by powder diffraction are corroborated by atom probe measurements. The second objective is to determine the competition in precipitation of S1 and S2 through observations of the formation kinetics as a function of temperature. *In situ* X-ray diffraction experiments have been performed for this purpose. Based on the kinetics of their transformation, some inferences regarding the mechanism of replacement of S1 by the equilibrium S2 phase can be made.

## 2. Experimental procedure

### 2.1. Materials and heat treatments

Three high purity Al—Cu—Mg alloys were investigated in this study. The first, which was used for the time-resolved synchrotron powder diffraction and atom probe tomography measurements, has a composition of Al—2.5Cu—1.5Mg (wt.%) (Al—1.1Cu—1.7Mg at.%), and is the same material studied in [8,25,26]. This alloy was sand cast from high-purity elements (99.99%), homogenised at 520 °C for 3 days, and hot rolled to a 3 mm thick sheet. For the diffraction measurements, the material was filed down and sieved to obtain a powder with particles in the size range 45–160 μm. This powder was encapsulated in an Ar-filled ampoule and solution-treated at 500 °C for 1 h, before being water quenched to room temperature (during which the ampoule was broken). Some of this material was then used directly for *in situ* aging experiments, while the remainder was divided into separate samples, re-encapsulated and isothermally aged at temperatures ranging from 250 to 400 °C for times between 9 and 1005 h. For the atom probe measurements, heat treatments (solution-treatment at 500 °C for 1 h, followed by water quenching and aging at 200 °C for 9 h) were performed on small blocks of material (roughly 10 × 10 × 3 mm in dimension), from which multiple tips were cut using electrostatic discharge machining (EDM).

Two higher solute containing alloys, Al—1.5Cu—2.0Mg at.% and Al—1.2Cu—2.3Mg at.%, were synthesised in order to increase the volume fraction of the S phase precipitates (and hence increase the diffraction signal) and allow the S1 phase to be examined in

greater detail using high-resolution neutron and X-ray powder diffraction. These compositions were selected to be close to the maximum concentration at which the Cu and Mg will dissolve completely into solid solution at the solution treatment temperature, as determined using the TCAL2 database in ThermoCalc [27]. These alloys were die cast from high purity elements (99.99%) and subsequently homogenised at 500 °C for 2 days, before being filed down and sieved to obtain powder samples with particles in the size range 45–160 μm. Solution-treatments were performed at 505 °C for 1 h using Ar-filled ampoules, which were again water quenched to room temperature. Samples were then re-encapsulated and isothermally aged at 300 °C for times between 1 and 336 h.

### 2.2. Atom probe tomography

Specimens for atom probe tomography (APT) were prepared from the alloy material after heat treatment by cutting small blanks (~0.4 mm × 0.4 mm × 15 mm) using EDM. Needle-like specimens for APT analysis, having fine tips (radius ~50–100 nm), were subsequently prepared using a standard two-stage electropolishing technique [28]. APT experiments were performed using a LEAP 4000 HR (CAMECA Instruments) with a voltage pulse repetition rate of 200 kHz, pulse fraction (the ratio of pulse voltage to DC standing voltage) of 20%, detection rate of 0.01 atoms per pulse and specimen temperature of ~20 K. Reconstruction and visualisation of the APT data was performed using the IVAS 3.6.6 software package, in combination with advanced reconstruction volume calibration techniques [29,30] based on measurement and comparison of lattice plane spacings in known crystallographic directions located at crystallographic poles observed in stereographic projection on the detector hit map.

### 2.3. High-resolution neutron and X-ray powder diffraction

Neutron powder diffraction measurements were performed on the High Resolution Powder Diffractometer (HRPD) [31,32] at the ISIS Pulsed Neutron and Muon Source (Rutherford Appleton Laboratory, UK). This instrument was selected for its exceptionally high peak resolution, which is needed in order to distinguish between the closely related unit cells of S1 and S2 (cf. Fig. 1). Diffraction data were collected under ambient conditions using the back scattering detector bank (168° $2\theta$) for three different time-of-flight windows, 10–100 ms, 30–130 ms and 100–200 ms, corresponding to $d$-spacing ranges of 0.3–2.15 Å, 0.65–2.50 Å and 2.15–3.9 Å, respectively. Approximately 6 g of each alloy powder (~3 $cm^3$) was loaded into the vanadium sample canisters in order to fill the volume illuminated by the neutron beam and hence maximise the diffraction signal. Acquisition times ranged from 8 to 12 h, depending on the time-of-flight window, to improve the counting statistics. This was necessary given the low concentration of the S1 phase (~6 wt.%) in the alloy samples and the low intensity of the incident neutron beam. Diffraction patterns were also collected from an equivalent volume of a standard material ($Y_2O_3$) in order to characterise the instrumental contribution to peak shape. The neutron data were normalised to the incident monitor spectrum and corrected for detector efficiency based on the scattering from a vanadium standard.

High-resolution X-ray powder diffraction patterns were collected from the same set of samples using the powder diffraction beamline at the Australian Synchrotron [33]. A monochromatic X-ray beam with a nominal energy of 18 keV was used, and data were collected over the angular range 1–81.5° $2\theta$ ($d$-spacing range of 0.6–30 Å) using the Mythen position sensitive detector in Debye–Scherrer transmission geometry [34]. Samples were packed into 0.5 mm diameter glass capillaries, which were continuously rotated about their axes at ~1 Hz in order to improve the particle statistics and hence help ensure accurate observed relative peak intensities. The diffraction patterns, which were acquired in pairs with the detector offset by 0.5° $2\theta$ in order to eliminate the gaps between the modules of the Mythen detector, were merged using the program CONVAS2 [35]. A precise determination of the X-ray wavelength ($\lambda$ = 0.688572 Å) was derived from diffraction data collected from a sample of $LaB_6$ (NIST SRM 660a) mixed with diamond powder.

### 2.4. In situ synchrotron powder diffraction

The kinetics of the transformation from S1 to S2 were investigated in a separate *in situ* synchrotron experiment conducted on the powder diffraction beamline at the Australian Synchrotron. The experimental setup and instrument calibration were the same as for the high-resolution measurements described above, although in this experiment a nominal X-ray energy of 15 keV was used. Samples of the solution-treated and quenched alloy powder were contained in sealed quartz glass capillaries, which were heated using a hot-air blower controlled by a thermocouple positioned directly beneath the capillary. Isothermal aging experiments were performed *in situ* at 250 °C, 300 °C, 350 °C and 400 °C, for aging times up to 12 h. The sample temperature was calibrated using the known phase transition (solid–solid and solid–liquid) temperatures of a range of standard materials, including $KNO_3$, $KClO_4$, $Ag_2SO_4$ and $SiO_2$, allowing the temperature to be controlled to ±3 °C. In order to heat the samples as rapidly as possible, the hot air blower was directed away from the sample while it was ramped up to the desired temperature. Data collection was then begun, allowing several data sets to be collected with the sample at room temperature, before the hot-air blower was repositioned beneath the sample using a motorised translation stage. This had the effect of heating the sample to the desired temperature in less than 2 s, as determined by the time taken for the thermal expansion of the α-Al lattice parameters to stabilise. *In situ* diffraction patterns were collected every 15 s for the first 2 min, every minute for the next hour, and every 5 min thereafter. A series of 60 *ex situ* samples, aged at the same temperatures used in the *in situ* experiments, but for times between 9 and 1005 h in the laboratory, were also examined (under ambient conditions), in order to explore the later stages of the S1 to S2 phase transformation.

### 2.5. Powder diffraction data analysis

The neutron and X-ray data collected from each of the high-solute samples were analysed simultaneously by the Rietveld method [36,37], as implemented in the Topas-Academic software package (version 4.1, Coelho Software, 2007). Empirical models for both the X-ray and neutron instruments were derived from patterns collected from standard materials ($Y_2O_3$, $LaB_6$ and Si). Each of the phases present in a given alloy sample were modelled using common structural parameters (lattice parameters, atomic coordinates, site occupation factors and atomic displacement parameters). However, independent scale factors and peak broadening functions (crystallite size and microstrain) were refined for the X-ray and neutron diffraction patterns. The *in situ* diffraction data were analysed using standard sequential Rietveld refinement. It should be noted that the errors reported for the parameters determined by Rietveld analysis are the estimated standard deviations (esds) calculated by Topas, and are likely to underestimate the true errors in the measurements [38]. These so-called "Rietveld errors" are based on the numerical fit to the data, and are provided here to give an impression of the stability of the refined parameters.

During the data analysis, anisotropic crystallite size broadening was observed for the S1 phase. In the previous study [8], this was modelled using a modified version of the March–Dollase preferred orientation algorithm [39], which assumes the crystallites are oblate spheroids. However, the S phase is well known to form with a lath morphology in Al—Cu—Mg alloys, with distinct length, width and thickness dimensions [6,8]. An ellipsoidal crystallite size function was therefore developed, to better account for this morphology. This ellipsoid function scales the crystallite size term in the Scherrer equation as follows:

$$\beta = \frac{\lambda}{f(hkl)L\cos(\theta)} \tag{1}$$

$$f(hkl) = \left((yz\cos(\varphi_{hkl})\sin(\phi_{hkl}))^2 + (xz\sin(\varphi_{hkl})\sin(\phi_{hkl}))^2 + (xy\cos(\phi_{hkl}))^2\right)^{-\frac{1}{2}} \tag{2}$$

where $\beta$ is the full width at half maximum of a Bragg peak, $\lambda$ is the wavelength, $L$ is the crystallite size parameter and $\theta$ is the diffraction angle. In the shape function $f(hkl)$, $x$, $y$ and $z$ are the principal axes of an ellipsoid with a volume equivalent to a unit sphere (i.e. $xyz = 1$), and $\varphi_{hkl}$ and $\phi_{hkl}$ are the angles made between the crystallographic direction $hkl$, and the $x$ and $z$ axes respectively. The parameters required to describe the shape of the ellipsoid can then be reduced to two ratios:

$$e_{yx} = \frac{y}{x}, \quad e_{zx} = \frac{z}{x} \tag{3}$$

$$x = \left(\frac{1}{e_{yx}e_{zx}}\right)^{\frac{1}{3}}, \quad y = e_{yx}\left(\frac{1}{e_{yx}e_{zx}}\right)^{\frac{1}{3}}, \quad z = e_{zx}\left(\frac{1}{e_{yx}e_{zx}}\right)^{\frac{1}{3}} \tag{4}$$

The principal advantage of this approach, over more sophisticated methods such as spherical harmonics [40], is that only three refinable parameters are required to model the size and shape of the S1 crystallites ($L$, $e_{yx}$ and $e_{zx}$), increasing the stability of the refinement. Note that this function can also be used to model spheres, plates and rods, by setting $e_{yx} = e_{zx} = 1$, $e_{yx} = 1$, and $e_{yx} = e_{zx}$ respectively.

## 3. Results

### 3.1. Difference between S1 and S2

High-resolution synchrotron X-ray and neutron powder diffraction patterns were collected from samples of two high-solute alloys (Al—1.5Cu—2.0Mg and Al—1.2Cu—2.3Mg at.%), in order to refine the crystal structure parameters of S1 and S2 using the Rietveld method [36]. Selected regions of the X-ray and neutron powder diffraction patterns collected from two Al—1.5Cu—2.0Mg (at.%) alloy samples aged for different times are shown in Fig. 2. It can be seen that both techniques have a similarly high level of peak resolution and are in excellent agreement, allowing the closely related S1 and S2 phases to be identified independently in both sets of data. In addition to the α-Al, S1 and S2 phases, these samples also contained small amounts (<1 wt.%) of θ phase ($Al_2Cu$) and MgO. The $Al_7Cu_2Fe$ phase was not observed in these samples, and the θ phase was primarily observed in the samples aged for 12 and 336 h (only trace amounts of θ were observed in samples aged for 1 and 4 h). Synchrotron diffraction patterns were also collected from the as quenched material, confirming that no S phase was present prior to the aging heat treatment.

The X-ray and neutron data collected from each sample were analysed simultaneously using common structural models for the various phases present (Section 2.5). Initially the atomic coordinates and site occupancies for both the S1 and S2 phases were fixed to the values reported by Heying et al. [24] for bulk equilibrium S phase, while other parameters (including atomic displacement parameters) were allowed to refine in order to achieve the best fit to the observed data. This process allowed the majority of the refinable parameters to stabilise close to their final values, and also provided benchmark $R_{wp}$ values which could be used to assess the improvement achieved by further refinement of the S1 and S2 structures.

Next the fractional atomic coordinates and site occupation factors for S1 and S2 were allowed to refine. In the six samples studied here, only the Al—1.5Cu—2.0Mg sample aged for 336 h contained a substantial amount of the S2 phase (3.5 wt.%). To minimise correlations between the structure parameters of S1 and S2, particularly in the samples aged for short times (1 and 4 h) where most of the S1 and S2 peaks are significantly overlapped, the atomic coordinates and site occupancies for S2 were refined for the 336 h sample and subsequently fixed during the analysis of the five other samples. The structure parameters for the S1 phase were allowed to refine for all six samples. Finally, the Al site occupation factors for both S1 and S2 were fixed to 1.0 (full occupation) to prevent strong correlations with the Rietveld scale factors. This is a reasonable assumption given the availability of Al atoms in this system. Fig. 3 highlights the excellent quality of fit obtained ($R_{wp}$ = 4.10%) by this approach for the sample containing the maximum concentration of S1.

The differences between the S1 and S2 crystal structure parameters obtained in this investigation are presented in Table 1, along with the values reported by Heying et al. [24] for comparison. The lattice parameters obtained for S1 and S2 are in good agreement with those observed previously for the Al—2.5Cu—1.5Mg wt.% alloy [8], indicating that the lattice parameters are not strongly dependent on the bulk alloy composition. The fractional atomic coordinates for both S1 and S2 deviated slightly from the values reported by Heying et al., although no clear trends were observed in the resulting atomic bond lengths. The Cu and Mg site occupation factors for S2 remained very close to 1.0, indicating that the composition of S2 is that of ideal S phase ($Al_2CuMg$). In comparison, the Cu and Mg site occupancies refined to 0.96 and 0.91, respectively, for the S1 phase, indicating a small deficiency in both elements in S1. Attempts to substitute Al atoms onto these sites by constraining the sites to be fully occupied by a mixture of Cu and Al, or Mg and Al resulted in a return to full site occupation by Cu or Mg (i.e. full occupation by Cu and Mg provided a better fit to the observed data than the partial substitution of Al atoms onto either site). This indicates that the deficiency is more likely to be the result of vacancies trapped in the S1 precipitates.

The Cu and Mg site occupancies obtained from the six samples studied in this investigation are summarised in Table 2. No significant differences were observed between the two alloy compositions studied. With the exception of the 336 h sample, the improvement in $R_{wp}$ due to structure refinement ranged from 0.08% to 0.15%. Although this improvement is small, it is significant given the low concentration and hence low peak intensity of the S phases present in the samples.

Previous investigations of the Al—2.5Cu—1.5Mg wt.% alloy have shown that the S1 phase forms as small, lath shaped precipitates with dimensions in the 5–50 nm range, while S2 forms as larger, more equiaxed particles [8]. To investigate the composition of the small S1 laths and corroborate the results of the powder diffraction-based structure refinements, APT measurements were made on samples of the Al—2.5Cu—1.5Mg alloy prepared in the peak aged state (200 °C for 9 h), where the number density of S1 precipitates is greatest (and hence maximise the chances of observing an S1 precipitate in the atom probe volume). This technique allows the type and location of millions of atoms to be determined over analysis volumes typically several hundred

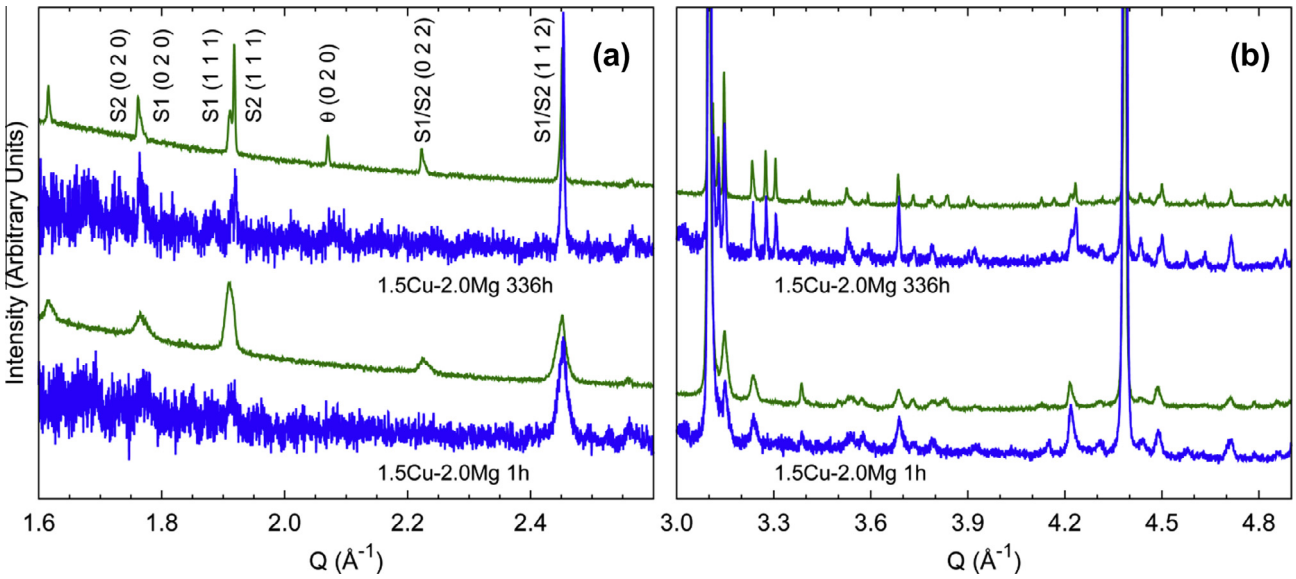


**Fig. 2.** Synchrotron X-ray (green) and neutron (blue) diffraction patterns collected from samples of the Al—1.5Cu—2.0Mg at.% alloy aged for 1 h (bottom pair) and 336 h (top pair). The X-ray and neutron data have been normalised to the intensity of the Al (1 1 1) peak. (a) and (b) correspond to regions of the neutron data acquired using the 100–200 ms and 10–100 ms time-of-flight windows respectively. (For interpretation of the references to colour in this figure legend, the reader is referred to the web version of this article.)

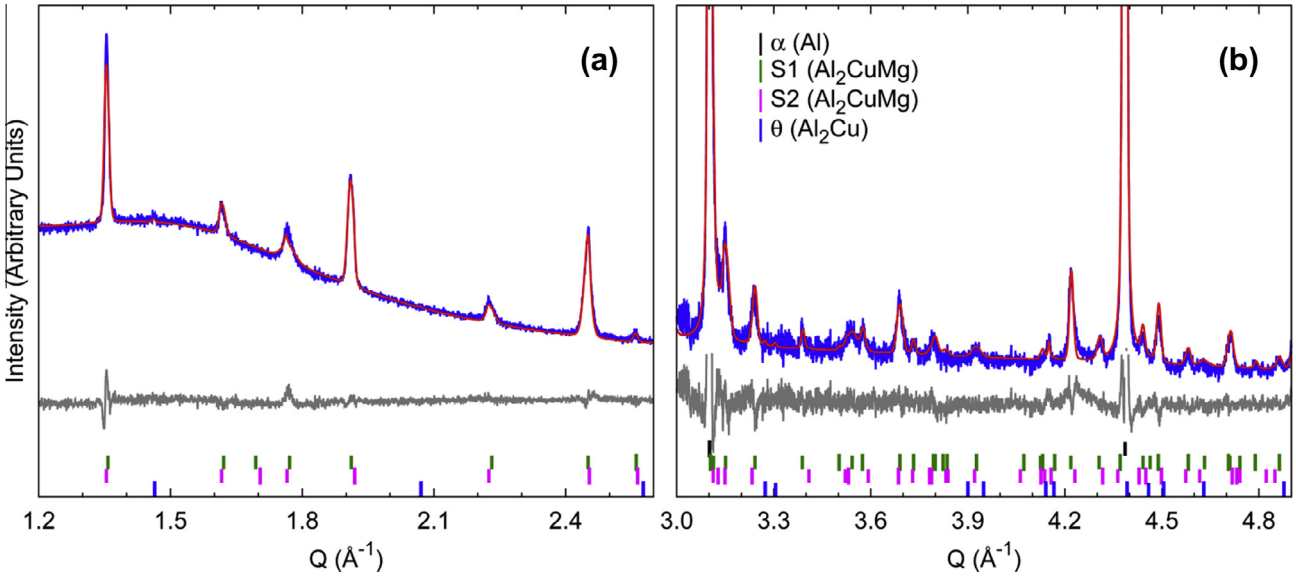


**Fig. 3.** Selected regions of the synchrotron (a), and neutron (b) diffraction patterns collected from the Al—1.5Cu—2.0Mg at.% alloy aged for 1 h. The observed, calculated and difference patterns are shown in blue, red and grey respectively, and *hkl* markers for the different phases are given at the bottom of both (a) and (b). (For interpretation of the references to colour in this figure legend, the reader is referred to the web version of this article.)

nanometres in length, and can be used to characterise the shape and composition of nano-scale precipitates. Cu, Mg and Si iso-concentration surfaces for a representative APT sample are shown in Fig. 4. Two precipitate populations can be seen, one with the characteristic lath shape and cross-sectional dimensions of the S phase, and another with a small rod-like morphology. Interestingly, despite the high purity of this material, there is a small amount Si present, which appears to segregate to the interface between the S phase lath and the α-Al matrix.

Proximity histograms (Fig. 5) derived from the APT data show that the lath-shaped precipitates have a composition close to $Al_2CuMg$, while the smaller rods have a composition of around $Al_4CuMg$. Based on their size, morphology and composition, these small rod-like precipitates are thought to be GPB zones, in agreement with previous studies [41,42]. Upon close inspection of the proximity histograms for the S phase laths there appears to be a slight deficiency of Cu atoms relative to Al and Mg. This is highlighted further by taking linear concentration profiles across the narrow dimension of the S phase lath (Fig. 6). These results appear to confirm the small deficiency in Cu concentration observed in the powder diffraction study, although confirmation of the Mg deficiency is less clear.

### *3.2. Kinetics of the transformation from S1 to the equilibrium S2 precipitate*

In order to characterise the replacement of the metastable S1 phase by the equilibrium S2 phase, an *in situ* synchrotron powder

**Table 1**
Refined crystal structure parameters for the S1 and S2 phases, based on data collected from the 1 h and 336 h samples respectively (i.e. maximum S1 and S2 concentrations). The structure parameters determined by Heying et al. [24] are included for comparison.

| Parameter | S1 | S2 | S (Heying et al. [24]) |
|---|---|---|---|
| *a* cell (Å) | 4.0478(2) | 4.0144(1) | 4.0119(9) |
| *b* cell (Å) | 9.2552(4) | 9.2677(1) | 9.265(2) |
| *c* cell (Å) | 7.0948(6) | 7.1234(1) | 7.124(1) |
| Site Al *y* | 0.3537(5) | 0.3553(6) | 0.3558(2) |
| Site Al *z* | 0.0538(6) | 0.0531(6) | 0.0556(2) |
| Site Cu *y* | 0.7809(3) | 0.7808(3) | 0.7801(1) |
| Site Mg *y* | 0.0624(9) | 0.067(1) | 0.0651(3) |
| Occupancy Al | 1.0* | 1.0* | 1.0 |
| Occupancy Cu | 0.96(2) | 1.00(1) | 1.0 |
| Occupancy Mg | 0.91(3) | 0.99(2) | 1.0 |
| $B_{eq}$ Al (Å$^2$) | 1.0(2) | 1.1(1) | 0.86(7) |
| $B_{eq}$ Cu (Å$^2$) | 1.08(8) | 1.26(7) | 0.45(2) |
| $B_{eq}$ Mg (Å$^2$) | 1.5(3) | 1.9(2) | 0.55(3) |

* Note that the Al site occupation factors were fixed to 1.0 to prevent strong correlations between site occupancies and the scale factor.

diffraction experiment was performed using the Al—2.5Cu—1.5Mg (wt.%) material for aging times up to 12 h. A series of *ex situ* samples were also studied, to investigate aging times between 9 and 1005 h.

The evolution of the (1 1 1) S phase peaks observed during the first 8 h of *in situ* aging is shown in Fig. 7. The peaks from both S1 and S2 appear very rapidly in all four data sets, with the S1 peak approaching its maximum intensity quickly whilst the S2 peak increases more gradually with time. In the data collected at higher temperatures (350 and 400 °C), peaks from the S1 and S2 phases are seen within 15 s of exposure to elevated temperature (i.e. in the first diffraction pattern), whilst for the 250 and 300 °C data sets, the first indication of S phase peaks appears after ~2 min and ~30 s respectively. Other minor phases observed in the *in situ* experiments include $Al_2Cu$ (θ phase), $Al_7Cu_2Fe$ and MgO (surface oxide). The $Al_2Cu$ and $Al_7Cu_2Fe$ phases occurred with maximum concentrations of 0.1 and 0.15 wt.% respectively during the 400 °C heat treatments, while the MgO concentration peaked at 0.8 wt.% at the same temperature.

The diffraction data were modelled using the Rietveld method [36], and the relative phase compositions for both the *in situ* and *ex situ* samples were calculated based on the Rietveld scale factors [43]. The resulting concentrations for the S1 and S2 phases are shown in Fig. 8. The S1 phase precipitates very quickly at all four temperatures studied, before being replaced by the S2 phase. Only the data collected at 250 °C show any sign of an incubation period (1–2 min) prior to the formation of the S1 phase (Fig. 8a). The maximum S1 concentration of ~4.8 wt.% is observed in this experiment after ~10 h of aging at 250 °C. As the aging temperature increases the peak S1 concentration progressively decreases, and occurs at shorter aging times down to as short as 6 min at 400 °C. S1 is completely replaced by the equilibrium S2 phase within 580 and 48 h at the high aging temperatures of 350 and 400 °C respectively. Fig. 8b shows that the S2 concentration continues to increase throughout the heat treatments. The small discrepancy between the *in situ* and *ex situ* data (particularly in the 300 °C dataset) is likely to be the result of a slight difference in temperature between the *in situ* setup and the muffle furnaces used to age the *ex situ* samples.

The total concentration of S phase (S1 + S2) in this alloy is limited by the amount of Cu available. Taking into account the solubility of Cu in the Al matrix at each of the aging temperatures, the theoretical maximum concentration of S (based on thermodynamic calculations using the TCAL2 database) is 5.35 wt.% (4.1 vol.%) at 250 °C, 4.99 wt.% (3.82 vol.%) at 300 °C, 4.22 wt.% (3.22 vol.%) at 350 °C, and 2.90 wt.% (2.2 vol.%) at 400 °C, respectively. This is in good agreement with the results shown in Fig. 8c, although the observed S phase concentration is slightly higher than predicted at 400 °C.

Comparison of the lattice parameters observed for the S1 and S2 phases reveals some significant differences in behaviour during aging. Fig. 9 plots the *b* and *c* lattice parameters observed during the *in situ* measurements, for both S1 and S2. The *b* lattice parameter of S1 increases markedly as time progresses (from start to end), whilst the *c* lattice parameter remains fairly constant at low temperatures and reduces slightly at higher temperatures. In comparison, the lattice parameters of the S2 phase remain remarkably constant, with the exception of a few early points when there is very little S2 present in the sample. These results are in qualitative agreement with those of Gupta et al. [3].

This difference in behaviour is further highlighted in Fig. 10, which shows the evolution of the α-Al, S1 and S2 *a* cell parameters over time for the 350 °C dataset. Note that the S1 cell parameter is very close to that of the α Al matrix (within 0.003 Å), and follows the evolution of the matrix lattice parameter. In comparison, the S2 *a* cell is markedly smaller than the α-Al matrix, and remains constant with time. For the *ex situ* samples the difference between the α-Al and S1 *a* lattice parameter is within 0.004 Å. Overall, the variations in the S1 lattice parameters result in an increase in the unit cell volume with aging time as shown in Fig. 11.

As in the previous *ex situ* investigation [8], anisotropic crystallite size broadening was observed for the S1 phase for all heat treatment times and temperatures. In this investigation, the morphology of the S1 crystallites was modelled using a tri-axial ellipsoid function (Section 2.5), which is a better approximation of the S1 laths than the oblate spheroid function used previously. The principal axes of the ellipsoid function were aligned with the lattice parameters of the S1 phase such that *x* is parallel to $[1\,0\,0]_{S1}$, *y* is parallel to $[0\,1\,0]_{S1}$, and *z* is parallel to $[0\,0\,1]_{S1}$. These directions correspond to the orthogonal length, width and thickness dimensions of the laths respectively. The resulting anisotropic crystallite size parameters refined from the *in situ* data are shown in Fig. 12. The crystallite size parameters increase continuously throughout the different heat treatments (including the 400 °C data set), and are in good agreement with the dimensions observed by TEM measurements [8] providing confidence in the values extracted from the refinement of the diffraction data.

**Table 2**
Weight fractions, site occupation factors and atomic displacement parameters ($B_{eq}$) refined for the S1 phase, based on the high resolution X-ray and neutron data. Alloy 1 = Al—1.5Cu—2.0Mg at.%, alloy 2 = Al—1.2Cu—2.3Mg at.%.

| Alloy | Time at 300 °C (h) | $R_{wp}$ (%) | S1 wt.% | S2 wt.% | S1 site occupation and atomic displacement | | | | | |
|---|---|---|---|---|---|---|---|---|---|---|
| | | | | | Al Occ | Al $B_{eq}$ | Cu Occ | Cu $B_{eq}$ | Mg Occ | Mg $B_{eq}$ |
| 1 | 1 | 4.10 | 5.6(2) | 0.9(1) | 1.0 | 1.0(2) | 0.96(2) | 1.08(8) | 0.91(3) | 1.5(3) |
| | 4 | 4.54 | 4.8(2) | 1.5(1) | 1.0 | 0.8(1) | 0.98(2) | 1.20(6) | 0.96(2) | 1.6(2) |
| | 12 | 4.54 | 4.5(2) | 1.7(1) | 1.0 | 0.9(2) | 0.96(2) | 1.1(1) | 0.95(3) | 1.8(3) |
| | 336 | 3.50 | 1.70(9) | 3.50(9) | 1.0 | 1.2(1) | 0.96(2) | 1.25(7) | 0.99(4) | 1.7(2) |
| 2 | 1 | 3.99 | 4.5(2) | 1.0(1) | 1.0 | 0.9(1) | 0.98(2) | 1.23(8) | 0.92(3) | 1.7(3) |
| | 4 | 3.95 | 3.8(2) | 1.6(1) | 1.0 | 0.9(2) | 0.98(2) | 1.29(9) | 0.98(3) | 1.8(3) |

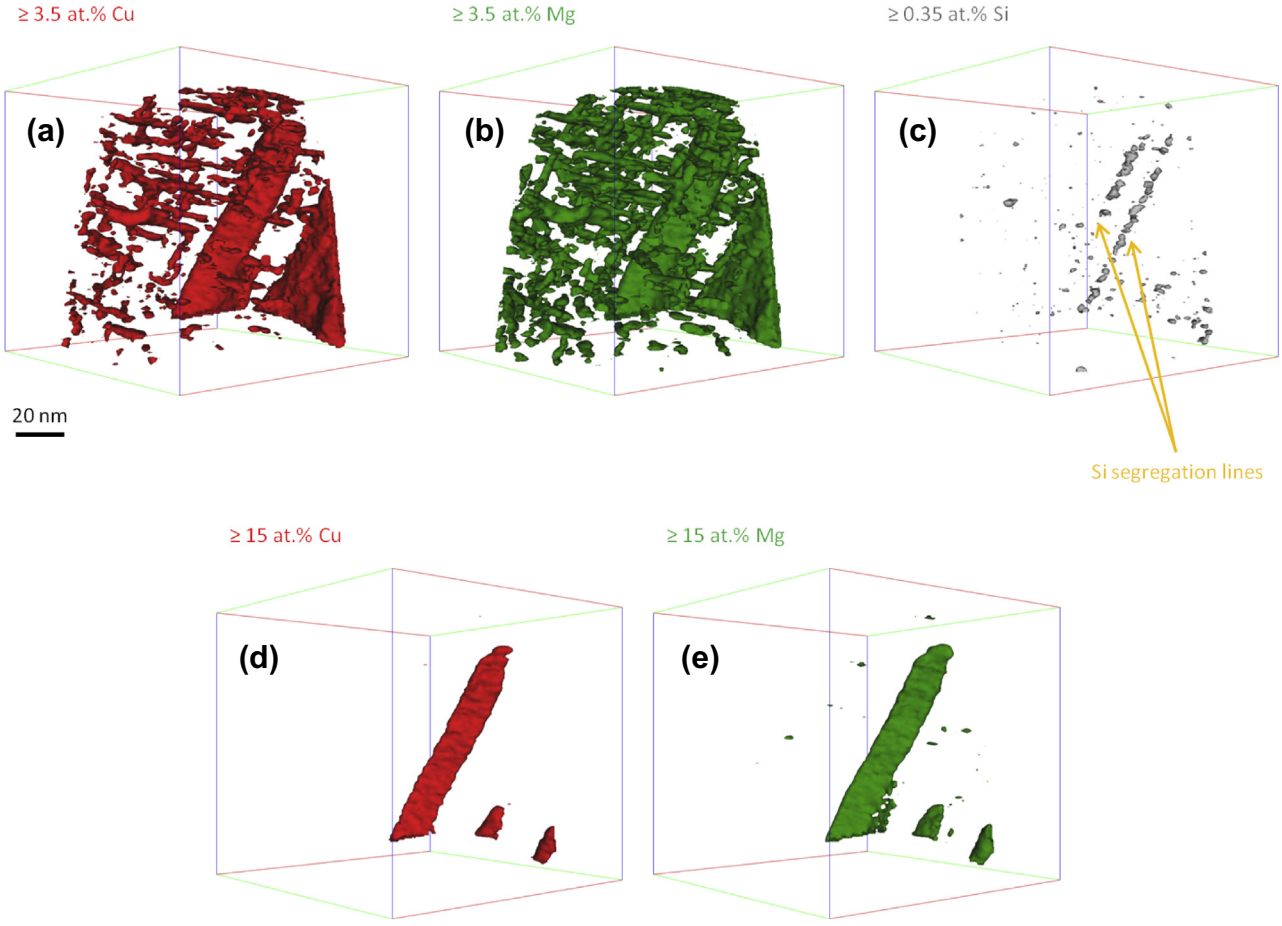


**Fig. 4.** Iso-concentration surfaces for (a) Cu, (b) Mg and (c) Si atoms, with concentrations greater than 3.5 at.%, within a sample aged at 200 °C for 9 h. (d) and (e) show similar iso-concentration surfaces for Cu and Mg respectively, with concentrations greater than 15 at.%.

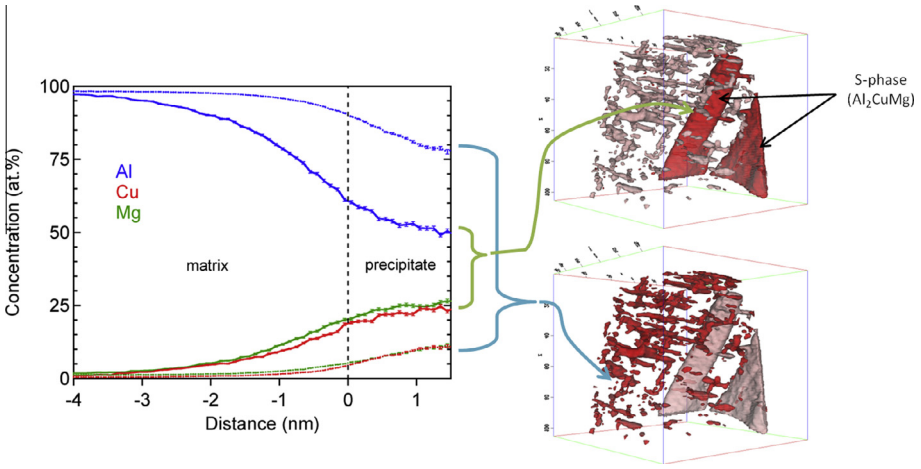


**Fig. 5.** Proximity histogram obtained by APT, showing the composition of the two precipitate populations across their interfaces with the α-Al matrix. The larger precipitates (top right) have compositions close to $Al_2CuMg$, corresponding to the S phase. The smaller rod shaped precipitates (bottom right) only contain ~12 at.% of Cu and Mg, and are likely to be GPB zones.

## 4. Kinetic analysis

The phase fractions and crystallite sizes determined during the Rietveld analysis of the *in situ* XRD data can be used to estimate the average number density of the S1 and S2 phases, the overall transformation kinetics of the two S phases, as well as the growth kinetics of the S phase. The evolution of the precipitate number density provides an insight into the nucleation, growth and coarsening stages of precipitation, and can be important to the interpretation of kinetic models. In order to calculate the number density,

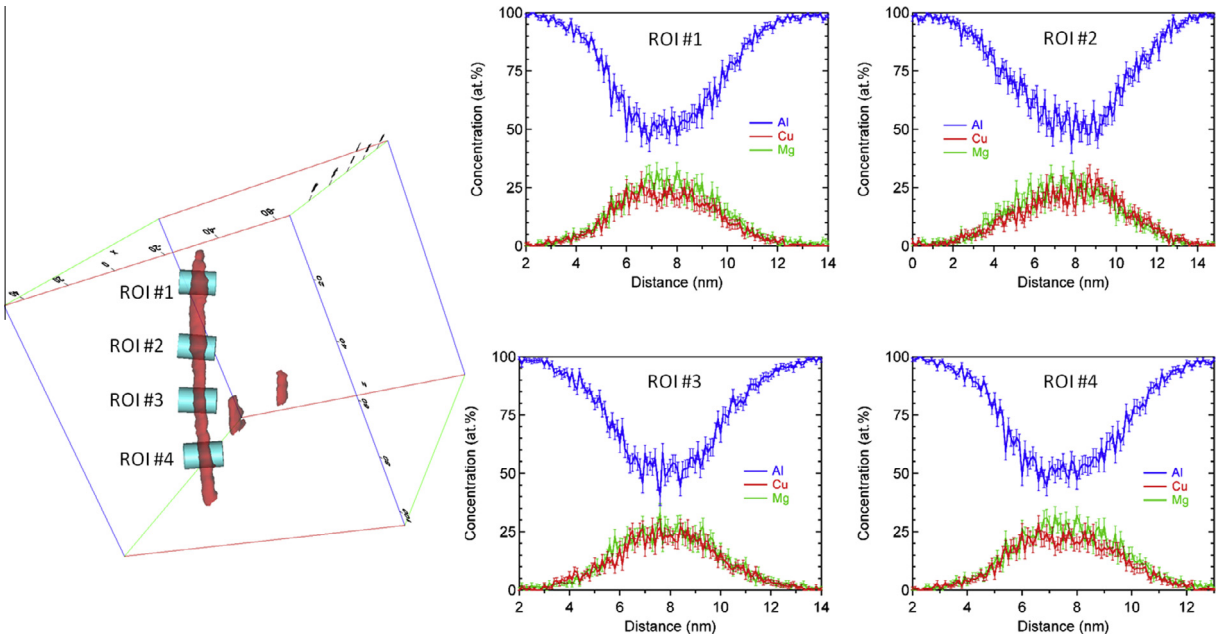


**Fig. 6.** Linear composition profiles taken across the narrow dimension of the S phase lath observed in the APT data, highlighting the small deficiency in Cu concentration.

the weight fractions determined during the quantitative phase analysis are converted into volume fractions. This can be done using equations of the form:

$$Vf_{S1} = \frac{Wf_{S1}}{Wf_{S1} + Wf_{S2} + \left(\frac{\rho_S}{\rho_{Al}}\right) \times Wf_{Al}} \tag{5}$$

where $Vf_i$, $Wf_i$ and $\rho_i$ are the volume fraction, weight fraction and density of phase $i$ respectively (neglecting the contribution of the other minor phases, and taking the average crystallographic density of the two S phases at a given temperature). The number density of the S1 and S2 precipitates can then be calculated by:

$$N_{S1} = \frac{Vf_{S1}}{V_{S1}} \tag{6}$$

where $V_i$ is the average precipitate volume for phase $i$ determined from the crystallite size parameters.

The evolution of the number density calculated for the S1 and S2 precipitates is shown in Fig. 13. From Fig. 13a it can be seen that the S1 number density passes through a maximum early during the aging process, in less than 15 min at 250 °C and even faster at higher temperatures, indicating that the nucleation of S1 is rapid. Soon after reaching the maximum, the number density decreases, with no prolonged period of constant number density indicative of a distinct growth stage. This suggests that the nucleation, growth and coarsening stages overlap significantly for the S1 phase. Although the S2 number density evolves more slowly (Fig. 13b), particularly in the case of the 250 °C sample, the calculated values do not plateau for a prolonged period either. This suggests that the nucleation, growth and coarsening stages of S2 also overlap.

It is important to highlight that the number density calculations presented here are estimates (particularly during the early stages of S2 formation), as they are derived from average crystallite size values. Crystallite size is a measure of the coherent domain size for diffraction, and as such, is always smaller than the true particle size. In addition, it is not possible gain any insight into the size distribution of the crystallites from the data presented here, due to the small phase fractions and significant peak overlap involved. However, the trends presented in Fig. 13 should be representative, and the maximum precipitate number densities of around $10^{21}$ to $10^{22}$ m$^{-3}$ for S1 are typical of precipitation in 2xxx alloys [44–48]. This lends further weight to the reliability of the values extracted from refinement of the X-ray data.

It is clear from the quantitative phase analysis that the S1 phase forms more rapidly, and hence must have a kinetic advantage over the formation of the S2 phase. In order to quantify this advantage, and gain a greater insight into the transformation mechanism, kinetic models can be applied to the results of the Rietveld analysis. There are a range of kinetic models for solid state transformations reported in the literature, the most well-known being the Johnson–Mehl–Avrami–Kolmogorov [49–53] (JMAK) model:

$$\alpha = 1 - \exp\left(-(kt)^n\right) \tag{7}$$

where $\alpha$ is the fraction transformed, $k$ is the rate constant dependent on the temperature, and $n$ is the so-called Avrami exponent. However, numerous investigations have shown that the JMAK model is not necessarily the most appropriate method for investigating precipitation mechanisms in alloy materials [54–59]. In particular, it has been shown that the effect of soft impingement (i.e. overlap of diffusion fields) may not be accounted for adequately in the JMAK model [60].

More recently, Starink and Zahra [58,60–64] have demonstrated that a model based on the Austin–Rickett equation [65], which includes an adjustable impingement factor, can provide a more reliable interpretation of the kinetic data.

$$\alpha = 1 - \left(\frac{(kt)^n}{n_i} + 1\right)^{-n_i} \tag{8}$$

where $n_i = 1/(\lambda_i - 1)$ is an adjustable impingement parameter. The term $\lambda_i$ corresponds to the strength of the impingement occurring within the system. For $\lambda_i = 0$ (no impingement), Eq. (8)simplifies to the general power law $\alpha = (kt)^n$. For $\lambda_i = 1$, Eq. (8)simplifies to the JMAK model (Eq. (7)). For $\lambda_i = 2$, Eq. (8)simplifies to the Austin–Rickett (AR) equation, with a stronger impingement effect. Fig. 14 shows the effect of the impingement parameter $\lambda_i$ and Avrami exponent $n$ on the shape of the transformation curve, for a fixed value of the rate constant $k$.

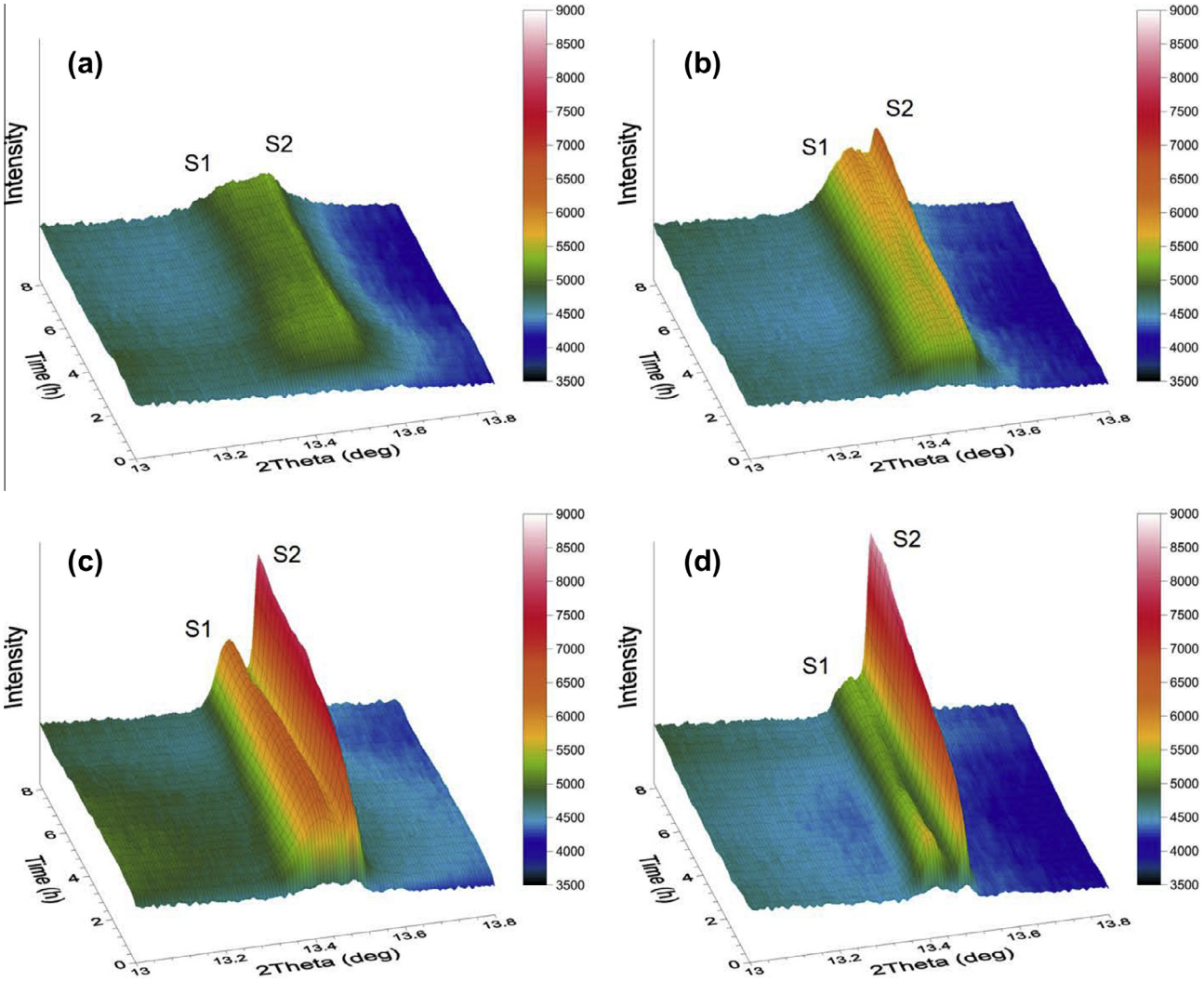


**Fig. 7.** Plots of accumulated diffraction patterns collected during *in situ* aging, showing the evolution of the $(1\,1\,1)_{S1}$ and $(1\,1\,1)_{S2}$ peaks. The data, which were collected at (a) 250 °C, (b) 300 °C, (c) 350 °C and (d) 400 °C, have been normalised to the incident beam monitor counts, and are plotted on the same intensity (colour) scale. (For interpretation of the references to colour in this figure legend, the reader is referred to the web version of this article.)

The Avrami exponent can also be partitioned according to:

$$n = N_{\mathrm{dim}} g + D \tag{9}$$

where $N_{dim}$ represents the dimensionality of the growing phase (1–3), $g$ is related to the growth mechanism ($\frac{1}{2}$ for diffusion controlled and 1 for interfacial growth), and $D$ depends on the nucleation rate (zero for existing nuclei and 1 for constant nucleation rate) [57,60].

In order to investigate the kinetics of the S1 and S2 precipitation, the Starink–Zahra (SZ) model has been applied to the results of the Rietveld analysis, by refining values for $\lambda_i$ as well as using fixed values corresponding to the power law (P), JMAK and AR models ($\lambda_i = 0$, 1 and 2 respectively). For the SZ model, $n$ was set to half integer values, ($n = \frac{1}{2}$, 1, $1\frac{1}{2}$, etc.), corresponding to fixed growth modalities (1D, 2D, 3D), assuming that the transformation mechanism is predominantly diffusion controlled growth of existing nuclei ($g = \frac{1}{2}$, and $D = 0$). This assumption is supported by the number density evolution in Fig. 13, which shows that S1 nucleation is very rapid. For the P, JMAK and AR models, the exponent $n$ was allowed to refine. Data were fitted over the range $0.1 < \alpha < 0.9$ where the rate of change is greatest. For S1, the transformed fraction ($\alpha_{S1}$) was calculated using the maximum concentration of S1 observed for each temperature series. For S2, $\alpha_{S2}$ was calculated using the maximum total concentration of S (i.e. S1 + S2) for each temperature, including the *ex situ* datasets (with the exception of the 300 °C *ex situ* data). The results of these analyses are presented in Table 3.

At 250 and 300 °C, the formation of the S1 phase is best fitted using the AR or SZ models, rather than the JMAK model, indicating that impingement effects play a significant role in the latter stages of formation, as expected. At 350 and 400 °C, the JMAK equation also began to fit the observed data quite well, whilst the AR model became less applicable and the values refined for the impingement parameter used in the SZ model decreased, suggesting that impingement becomes less important at higher temperatures. In comparison, the formation of S2 is well modelled by the JMAK equation at all temperatures, indicating that impingement effects are less important during the transformation of S1 to S2. At low temperatures, where the maximum transformed fraction observed is less than 50%, the formation of S2 is also well modelled by the power law. However, at higher temperatures, the *ex situ* samples reveal a reduction in the transformation rate, which suggests that JMAK is the more appropriate model overall. Fig. 15 shows examples of the fits obtained to the S1 and S2 transformation data using the AR and JMAK models, respectively.

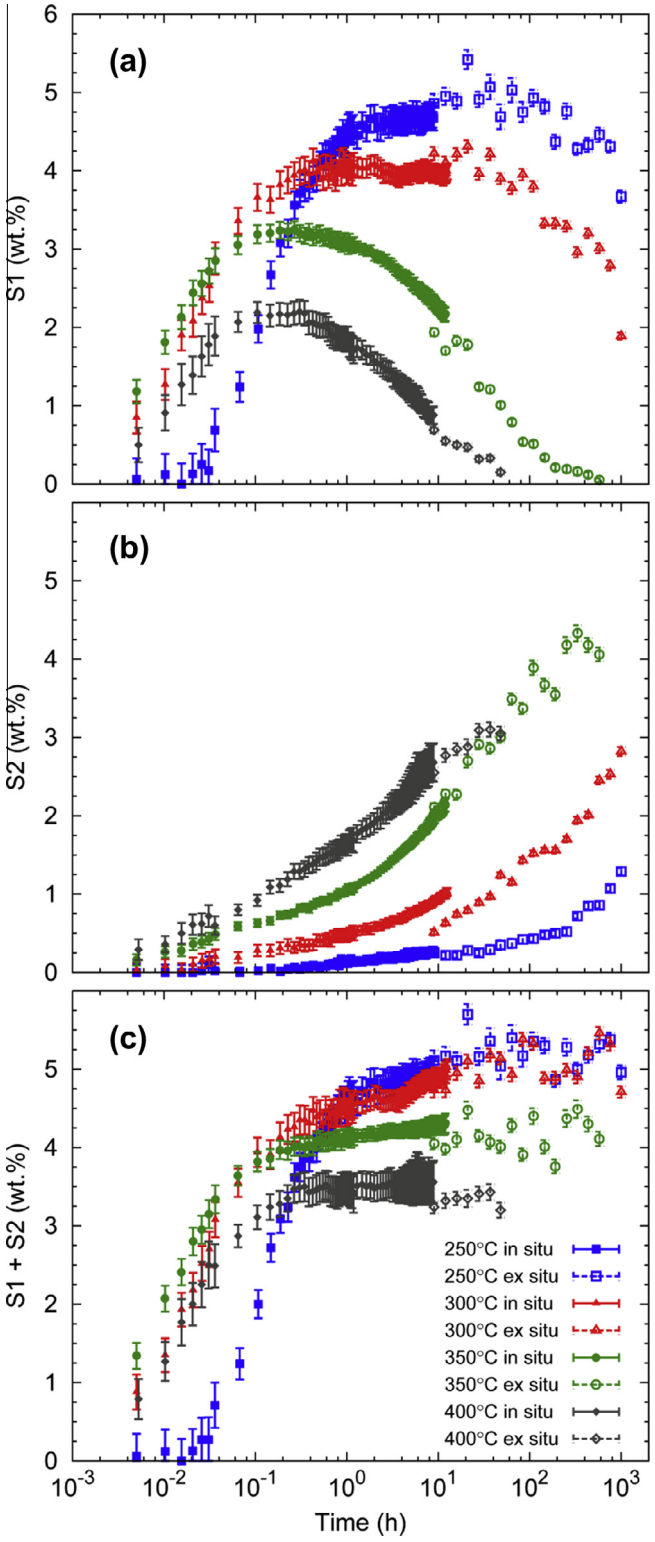


**Fig. 8.** Results of the quantitative phase analysis (using the method of [43]), showing (a) the transient formation of the S1 phase, (b) the progressive growth of the S2 phase, and (c) the overall concentration of S phase (S1 + S2) within the sample.

For S1, the values of the Avrami exponent $n$ were generally found to be in the range 1–1.5 for the best fitting models, which, according to the relation given in Eq. (9), is consistent with an average growth mechanism somewhat between 2D and 3D. This is in good agreement with the anisotropic growth of the S1 crystallites shown in Fig. 12, where growth along the [001] direction is significantly slower than growth in the other two directions. For S2, the values refined for $n$ were in the range 0.3–0.4, which would appear to correlate with a 1D growth mechanism. However, similarly low exponents have been observed during the growth and coarsening of precipitates located on heterogeneous sites such as grain boundaries and dislocations [66–69]. Given the lattice dimensions of S2, and the incoherent interface often observed between the equilibrium S phase and α-Al matrix, it would seem reasonable to suggest a similar growth mechanism may be responsible.

When applying the SZ models, the exponent $n$ was fixed to the half integral values 0.5, 1.0 and 1.5, corresponding to strictly 1D, 2D and 3D growth respectively, allowing the effect of the impingement parameter to be investigated. In general, the impingement parameter $\lambda_i$ refined to values between 1 and 2 for the S1 transformation, indicating that impingement within this system is greater than that accounted for using the JMAK equation, but (generally) less than that in the AR model. This is expected since soft impingement of diffusion fields will occur during the diffusion controlled growth of precipitates.

The rate constants $k$ refined in the kinetic analysis can be used to determine the average activation energy ($E_a$) for the formation of S1 and S2 using an Arrhenius relationship of the form:

$$k = k_0 \exp\left(\frac{-E_a}{RT}\right) \tag{10}$$

where $k_0$ is the pre-exponential factor, $R$ is the universal gas constant, and $T$ is the absolute temperature. The quantity $E_a/R$ can be determined from the slope of an Arrhenius plot, as shown in Fig. 16. The rate constants derived for S1 and S2 using each of the 5 models were analysed in this fashion, and the resulting activation energies are presented in Table 4. It should be noted that the data collected for S1 at 400 °C were excluded from this analysis, due to the substantially lower value of $k$ than expected, which is thought

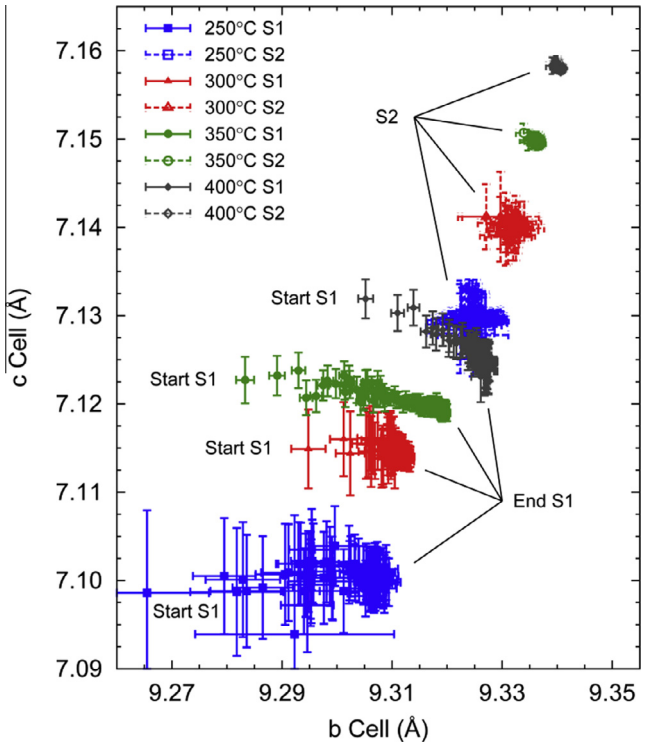


**Fig. 9.** *b* and *c* lattice parameters of the S1 and S2 phase obtained from the *in situ* experiments, illustrating the evolution with aging time.

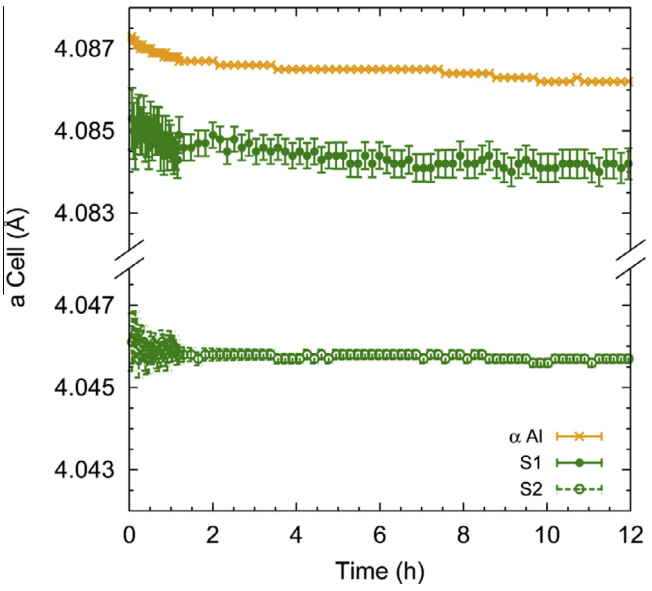


**Fig. 10.** *a* cell parameter of the α Al, S1 and S2 phases plotted against time for the 350 °C data set. The data collected at other temperatures exhibit similar behaviour.

to be an artefact of the significant overlap between the S1 and S2 formation at this temperature (the maximum concentration of S1 is considerably lower at 400 °C, which affects the calculation of the transformed fraction $\alpha_{S1}$).

For S1, all five of the models produced similar activation energies of between 73 and 78 kJ/mol. In this case, the power law model may be considered as an outlier, due to its poor ability to fit the observed data, and the SZ model using the high value for $n$ (1.5) is less consistent than the remaining three. For these reasons it is thought that the activation energy for S1 is closest to 75 kJ/mol.

For S2, there was a greater spread in activation energies. The power law model gave an activation energy of 137 kJ/mol, which is in good agreement with the known activation energies for diffusion of Cu and Mg in an Al matrix (136 and 131 kJ/mol respectively [70]). The JMAK and SZ models gave activation energies of 176 and 171 kJ/mol, which is significantly higher. It is unclear from the data which of these three models is most appropriate, however, it would appear that the activation energy for S1 formation is around half of that required for S2 formation, and half the value for Cu or Mg diffusion in the Al matrix, which is a surprising observation.

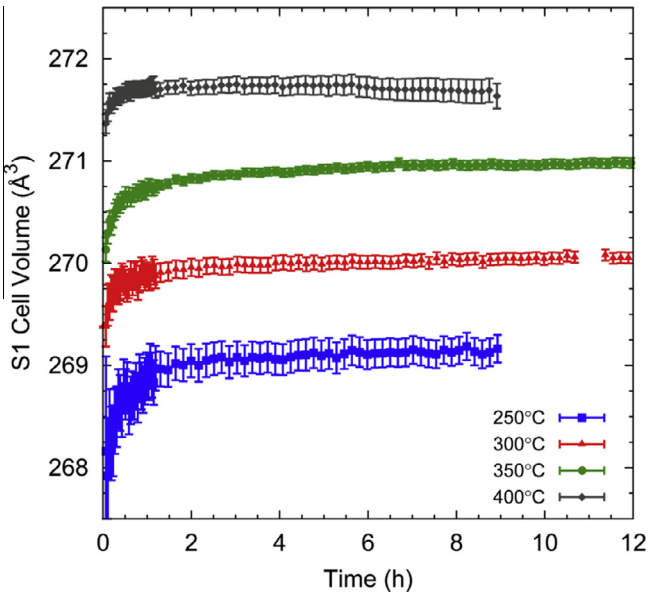


**Fig. 11.** Evolution of the S1 cell volume with time for the 4 temperatures studied here. Note that the offset between the cell volumes is due to thermal expansion.

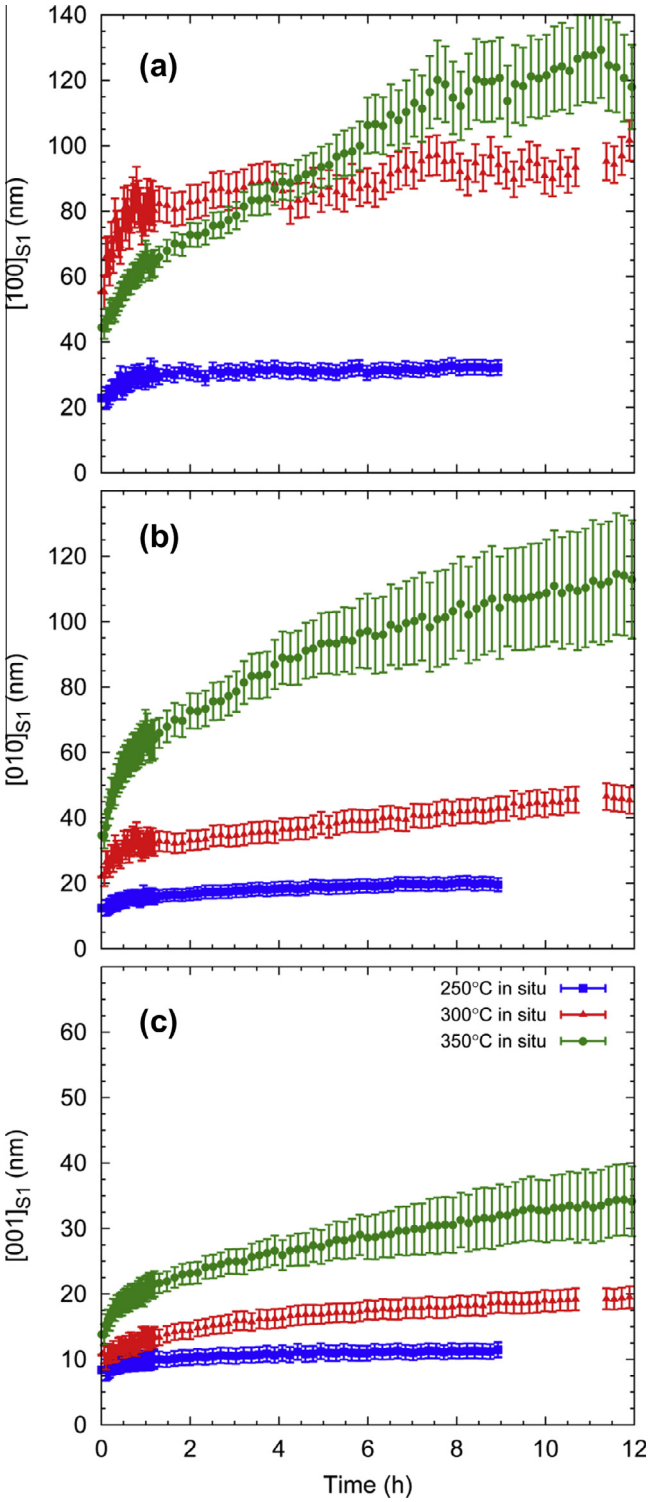


**Fig. 12.** Anisotropic crystallite size parameters for the S1 phase, refined using a triaxial ellipsoid model. The long axis of the ellipsoid is orientated parallel to the $[100]_{S1}$ direction, while the narrow axis orientated parallel to the $[001]_{S1}$ direction. 400 °C data omitted for clarity.

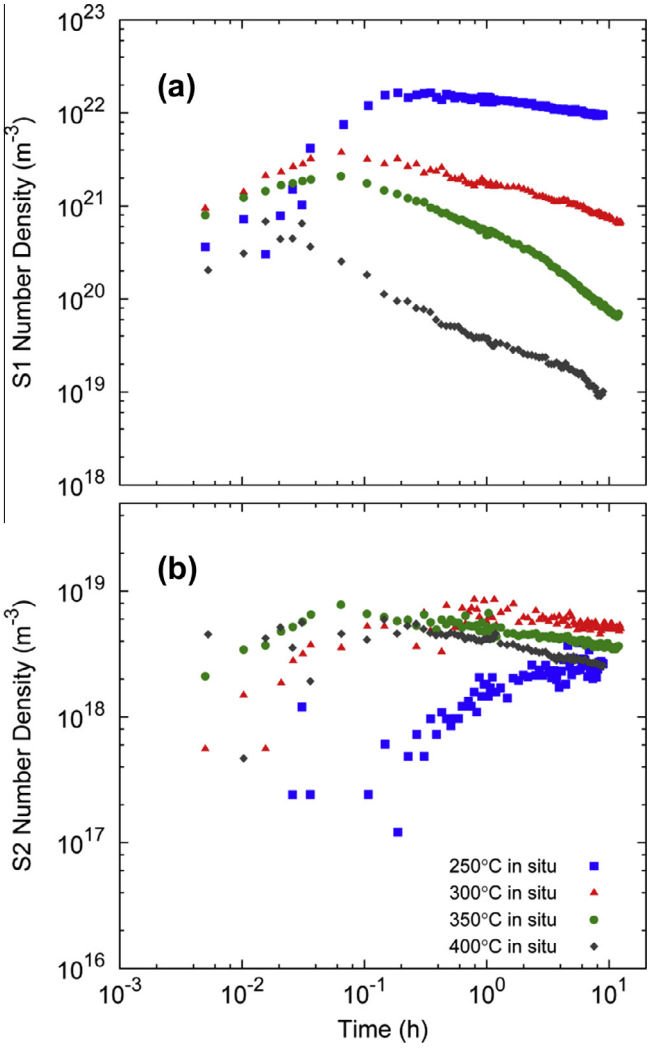


**Fig. 13.** Estimated precipitate number densities for (a) S1 and (b) S2, calculated from the phase fractions and crystallite size values refined during the Rietveld analysis of the *in situ* XRD data. The absence of plateaus indicates that the nucleation, growth and coarsening stages overlap.

An alternative approach to evaluating the average activation energy for S1 formation is to estimate the temperature dependence of the diffusivity of Cu in the alloy, back-calculated from the precipitate growth rate, which can be approximated using the observed crystallite size dimensions. The diffusion controlled lengthening of solute-rich precipitate plates, growing into a uniform, far-field solute containing matrix can be calculated using the Zener–Hillert equation [71]:

$$v = \frac{dl}{dt} = \frac{D}{2r}\left(\frac{C_o - C_e}{C_\beta - C_e}\right) \tag{11}$$

where $D$ is the diffusivity, $r$ is the radius at the edge of the lengthening precipitate plate, $C_o$ is the bulk (far-field) composition, $C_\beta$ is the concentration of solute (Cu) in the precipitate, and $C_e$ is the temperature dependent local equilibrium composition of the matrix at the moving interface.

In order to obtain the rate of plate lengthening, $dl/dt$, linear fits were applied to the S1 crystallite growth along the [1 0 0] direction over the initial period of aging where the S1 concentration is increasing and the concentration of Cu in the bulk is close to that of the original solid solution. The resulting fits are shown in Fig. 17. The minimum radius at the tip of the growing precipitate can be obtained from the ellipsoidal crystallite size model by calculating the focal point in the *a*–*c* (0 1 0) plane. By taking the average of the minimum radius over the same time period used to determine $dl/dt$, the diffusivity can be back-calculated using calculated values for $C_o$, $C_\beta$ and $C_e$. The results of this analysis are presented in Table 5. An Arrhenius plot of the diffusivity values (equivalent to that shown in Fig. 16) yields an activation energy of 64.4 kJ/mol, which is in reasonably good agreement with the values obtained from the quantitative phase analysis (~75 kJ/mol). Remarkably, the back-calculated diffusivities for Cu are between 4 and 5 orders of magnitude faster than the expected values, highlighting the surprising speed of the formation of S1.

## 5. Discussion

The powder diffraction data presented in Section 3 indicate that S1 is slightly deficient in Cu, at least during the early stages of aging, and is possibly slightly deficient in Mg as well. During the *in situ* experiments, the lattice parameters of S1 evolve over time, with both the *a* and *b* parameters tending toward (but not reaching) those of the equilibrium S2 phase, and the expansion of the *b* lattice parameter in particular causing a significant increase in the volume of the S1 unit cell. Conversely, the unit cell of the α-Al matrix decreases with aging time, as a consequence of the loss of solute from solution. These results could suggest the filling of vacancies in the S1 structure by Cu and Mg.

Despite the tendency of the *a* and *b* lattice parameters of S1 to move slightly towards those of S2 over time, the diffraction peaks of S1 and S2 remain distinct throughout the entire transformation. The S1 peaks do not merge gradually into those of the S2 phase, indicating that the transformation mechanism is not simply the gradual loss of coherency with the α-Al matrix as the precipitates grow in size. S1 and S2 are distinct phases.

In addition to monitoring the evolution of the S1 and S2 lattice parameters, the *in situ* X-ray diffraction experiments have allowed quantification of the transformed fractions and the crystallite sizes of the two S phases as functions of isothermal aging time. This is the first time such measurements have been reported in the

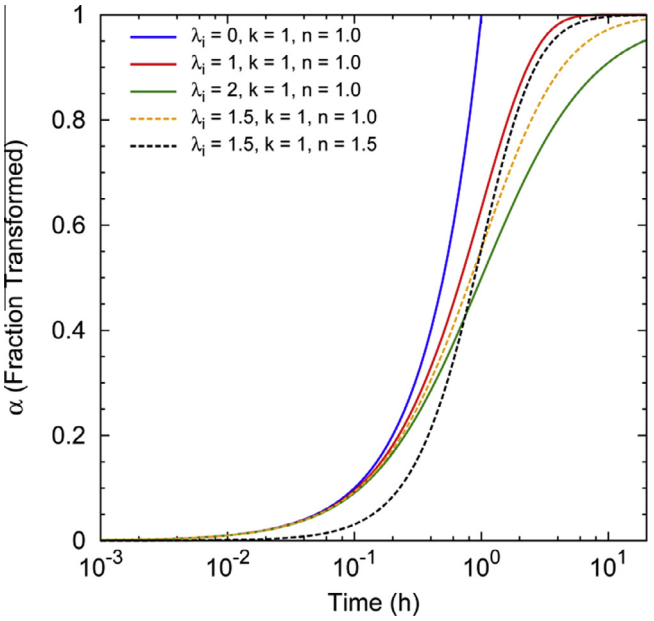


**Fig. 14.** Comparison between the different kinetic models employed in this investigation. Note that the power law ($\lambda_i = 0$) does not asymptote to $\alpha = 1$ like the other models. The impingement parameter $\lambda_i$ has a strong influence on the shape of the curve in the later stages of the transformation, while the Avrami exponent *n* influences the slope of the curve.

**Table 3**
Results of applying the SZ model to the results of the Rietveld analysis, using a range of different fixed and variable $\lambda_i$ and $n$ values. The quality of fit can be assessed by the resulting $R^2$ values.

| Temp | Model | S1 | | | | S2 | | | |
|---|---|---|---|---|---|---|---|---|---|
| | | $\lambda_i$ | $n$ | $k$ | $R^2$ | $\lambda_i$ | $n$ | $k$ | $R^2$ |
| 250 °C | P | 0 | 0.412 | 1.399 | 0.907 | 0 | 0.405 | $2.23 \times 10^{-5}$ | 0.960 |
| | JMAK | 1 | 0.914 | 4.679 | 0.952 | 1 | 0.425 | $3.36 \times 10^{-5}$ | 0.957 |
| | AR | 2 | 1.386 | 7.705 | 0.994 | 2 | 0.449 | $5.10 \times 10^{-5}$ | 0.953 |
| | SZ low $n$ | 1.371 | 1 | 6.046 | 0.985 | 3.015 | 0.5 | $9.26 \times 10^{-5}$ | 0.947 |
| | SZ high $n$ | 2.217 | 1.5 | 8.260 | 0.995 | 20.611 | 1 | $2.86 \times 10^{-3}$ | 0.891 |
| 300 °C | P | 0 | 0.344 | 6.436 | 0.911 | 0 | 0.306 | $4.19 \times 10^{-4}$ | 0.992 |
| | JMAK | 1 | 0.721 | 29.854 | 0.982 | 1 | 0.331 | $8.72 \times 10^{-4}$ | 0.991 |
| | AR | 2 | 1.118 | 51.899 | 0.991 | 2 | 0.358 | $1.66 \times 10^{-3}$ | 0.990 |
| | SZ low $n$ | 1.722 | 1 | 46.174 | 0.991 | 6.541 | 0.5 | $1.50 \times 10^{-2}$ | 0.984 |
| | SZ high $n$ | 2.808 | 1.5 | 66.234 | 0.985 | 19.497 | 1 | $2.35 \times 10^{-1}$ | 0.972 |
| 350 °C | P | 0 | 0.404 | 21.209 | 0.980 | 0 | 0.250 | $3.76 \times 10^{-3}$ | 0.977 |
| | JMAK | 1 | 0.757 | 71.563 | 0.998 | 1 | 0.371 | $2.68 \times 10^{-2}$ | 0.984 |
| | AR | 2 | 1.200 | 119.588 | 0.993 | 2 | 0.494 | $7.63 \times 10^{-2}$ | 0.966 |
| | SZ low $n$ | 1.550 | 1 | 98.913 | 0.997 | 1.758 | 0.5 | $6.61 \times 10^{-2}$ | 0.968 |
| | SZ high $n$ | 2.553 | 1.5 | 140.020 | 0.988 | 5.712 | 1 | $4.29 \times 10^{-1}$ | 0.898 |
| 400 °C | P | 0 | 0.609 | 22.798 | 0.982 | 0 | 0.214 | $2.60 \times 10^{-2}$ | 0.986 |
| | JMAK | 1 | 1.028 | 52.261 | 0.996 | 1 | 0.335 | $2.44 \times 10^{-1}$ | 0.994 |
| | AR | 2 | 1.512 | 78.410 | 0.989 | 2 | 0.470 | $7.99 \times 10^{-1}$ | 0.985 |
| | SZ low $n$ | 1.437 | 1 | 70.009 | 0.964 | 2.108 | 0.5 | $8.65 \times 10^{-1}$ | 0.984 |
| | SZ high $n$ | 1.909 | 1.5 | 75.829 | 0.990 | 5.042 | 1 | $3.58 \times 10^{0}$ | 0.948 |

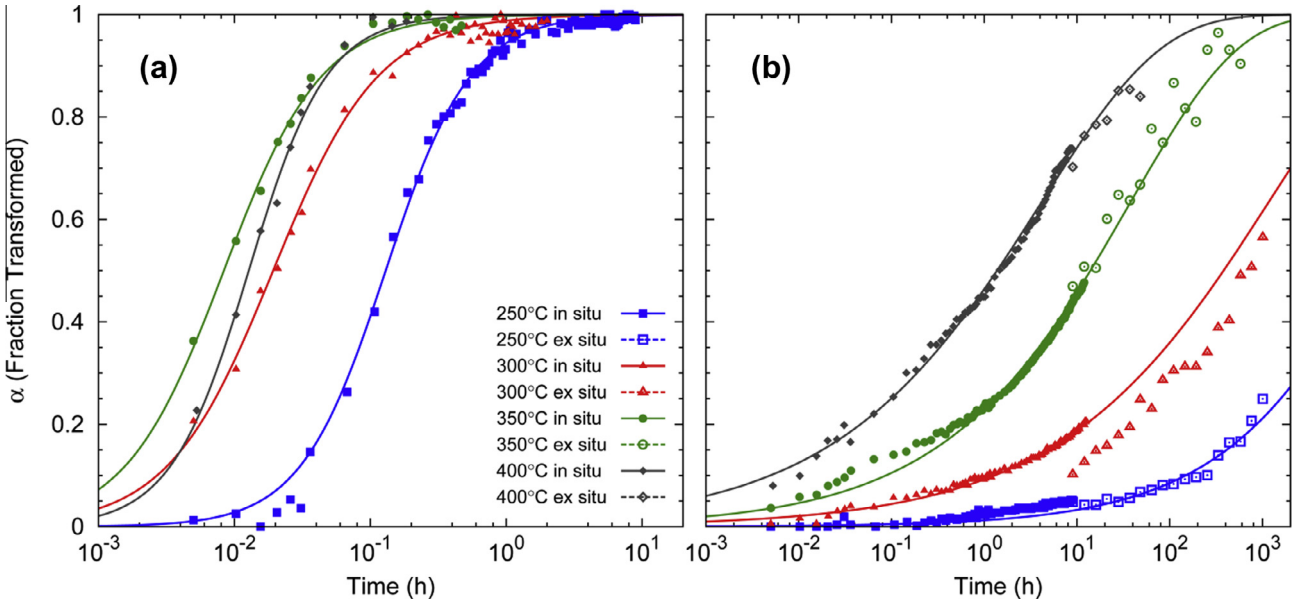


**Fig. 15.** Fraction transformed as a function of time for (a) S1 and (b) S2, fitted using the AR and JMAK models respectively. Note that the 300 °C *ex situ* data have been excluded from the analysis, due to the suspected discrepancy between the temperature of the *in situ* and *ex situ* samples.

literature, and given the importance of the S phase in 2xxx series alloys, the kinetic measurements are worth reporting.

The S1 phase grows surprisingly quickly at all of the temperatures studied in this investigation. Kinetic analysis of the diffraction data has revealed that the activation energy is significantly lower than that of Cu and Mg diffusion in an Al matrix. Analyses based on both the evolution of the average S1 crystallite size, as well as that of the overall transformed fractions give similar results. The Al—Cu—Mg system is well known for its ability to age naturally at ambient temperature (commercial alloys such as 2024 are often used in the naturally aged, T4 condition [72]). Following the quench from the solution heat treatment, studies have shown that small Cu and Mg clusters, as well as GPB zones will form at room temperature, creating chemical heterogeneities within the material [73–76]. Nuclear magnetic resonance results have also shown that nano-scale structures with Cu arrangements similar to the S phase can start to occur at room temperature [73]. Given that the samples for *in situ* analysis were prepared several days ahead of the synchrotron experiment and stored at room temperature, it is likely that GPB zones or similar chemical heterogeneities were present in the starting material, and the atom probe results (Fig. 4) show the GPB zones clearly. Such features could have provided the necessary solute for the S1 phase to nucleate quickly and to supply the solute for S1 phase growth. This would mean that the S1 phase is not growing into a uniform far field solute concentration, as is assumed by the Zener-Hiller equation and could explain the surprisingly fast Cu or Mg diffusion back-calculated using this approach. This kinetic analysis

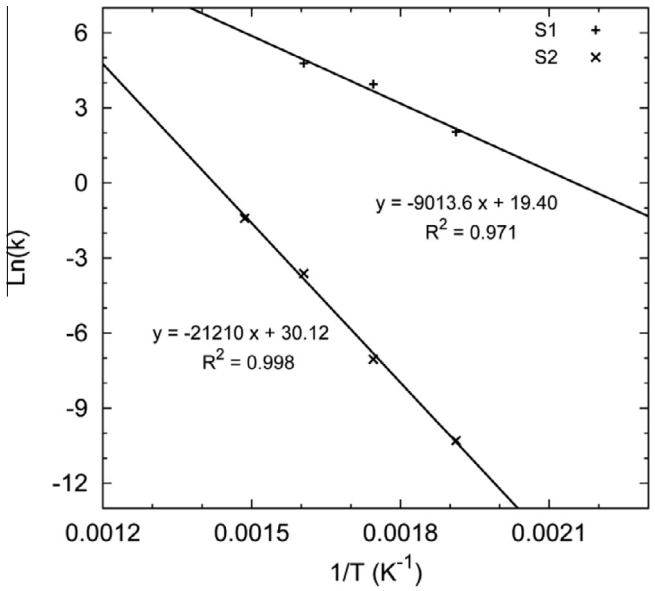


**Fig. 16.** Arrhenius plot of the rate constants for S1 and S2, derived using the AR and JMAK models respectively. The corresponding activation energies for S1 and S2 were found to be 75 and 176 kJ/mol.

highlights the important role GPB zone formation has on the subsequent kinetics of S phase formation.

The dimensions of the S1 crystallites are observed to grow fastest along the [1 0 0] and [0 1 0] directions, which correspond well with the lath morphologies observed by TEM, and with the mixture between 2D and 3D growth modes indicated by the kinetic analysis. The rapid nucleation and growth of S1 is likely assisted by the semi-coherence between the *a*-*b* plane of the laths and the α-Al matrix, with its correspondingly lower interfacial energy. However, this coherence could restrict the growth of the S1 phase later in the transformation as the precipitate size increases. This restriction could contribute to the higher degree of impingement observed in the kinetic analysis.

When considering the replacement of S1 with S2, there are several important items to note. The composition of the two phases are very close, so the influence of compositional gradients between the two precipitate populations is likely small. The total S phase concentration (S1 + S2) quickly reaches a maximum at all temperatures, and remains relatively constant over time, so the S1 to S2 transformation could be approximated as a form of coarsening reaction, occurring at constant total volume fraction. However, the crystallite size parameters for S1 were found to increase continuously throughout the transformation, with no indication that the precipitates were shrinking in size. Although the data presented here cannot provide any information regarding the S1 size distribution, the continuous increase in average S1 crystallite size would appear to rule out traditional Ostwald ripening where the equilibrium S2 phase grows at the expense of S1 by S1 dissolving and feeding solute through the matrix to S2. A possible explanation is that as the S1 precipitates grow, S2 nucleates heterogeneously on the S1/α-Al interface, where upon they absorb the S1 precipitate via a moving interface through the precipitate. While this is occurring, the two different crystallite domains would continue to contribute to the diffraction signals of the S1 and S2 phases. This hypothesis is supported by one of the high resolution TEM micrographs from the work of Winkelmann et al. [6], in which an S phase particle comprised of two regions with different lattice orientations was observed, as shown in Fig. 18. The lath shaped region in the bottom left of Fig. 18 would be consistent with S1 and the more equiaxed cross-section in the top right of Fig. 18 would be consistent with the expectations of the equilibrium S2 phase. The S2 phase may consume the metastable S1 by the migration of an internal S1/S2 interface (i.e. no long-range diffusion is involved) and such an explanation would be consistent with the success of the JMAK equation in describing the kinetics of S2 formation. It is clear that further work, involving a multi-technique approach, is required to fully understand the S1 to S2 transition.

Finally, it is worth reflecting on the importance of the S1 phase in this system, and the appropriateness of distinguishing it from the S2 phase. The results presented here show the structure and chemistry of the S1 and S2 phases are similar, however, the results also show that the two phases exist as distinct populations with different sets of lattice parameters, and not as a single phase with a spectrum of lattice parameters. The S1 phase forms considerably faster than S2, with an activation energy of around half that required for S2 formation, and the morphology of S1 is markedly different from that of S2 throughout the transformation process. The maximum concentration of the S1 phase occurs within the first ~9 h of aging at 250 °C, and the peak number density within the first hour. This time period corresponds closely to the peak aged condition for this alloy, and therefore S1 is clearly important to the physical properties. For these reasons, it would seem quite reasonable to classify S1 and S2 as distinct phases.

**Table 4**
Activation energies calculated for the formation of S1 and S2 using the 5 different kinetic models. Note that the activation energies obtained for S1 are very consistent, around 75 kJ/mol, while the values for S2 show a wider spread.

| Model | S1 | | S2 | |
|---|---|---|---|---|
| | $E_a$ | $R^2$ | $E_a$ | $R^2$ |
| P | 73.7 | 1.000 | 137.2 | 0.999 |
| JMAK | 74.5 | 0.977 | 176.4 | 0.998 |
| AR | 74.9 | 0.971 | 192.2 | 0.997 |
| SZ low *n* | 76.5 | 0.958 | 171.1 | 0.963 |
| SZ high *n* | 77.5 | 0.954 | 130.6 | 0.927 |

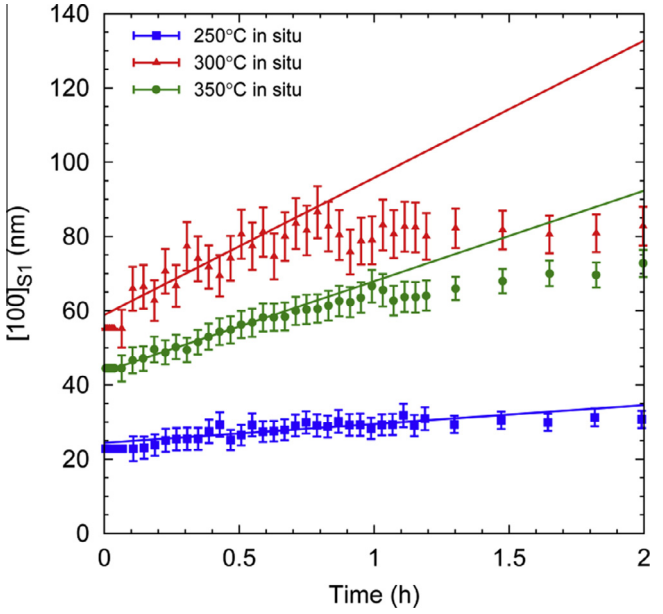


**Fig. 17.** Rate of S1 precipitate growth along the [1 0 0] direction, fitted using a linear approximation over the period where the S1 concentration is increasing.

**Table 5**
Parameters used to calculate the diffusivity of Cu, based on the rate of growth of the S1 crystallite size in the [100] direction. The values for $C_o$ and $C_\beta$ were, 0.011 and 0.25 respectively, giving an activation energy of 64.4 kJ/mol for S1 formation.

| Temperature | $dl/dt$ (m/s) | $r$ min (nm) | $C_e$ | $D$ ($m^2$/s) | |
|---|---|---|---|---|---|
| | | | | Calculated | Theory |
| 250 °C | $9.155 \times 10^{-6}$ | 0.853 | $3.20 \times 10^{-4}$ | $3.651 \times 10^{-13}$ | $1.699 \times 10^{-18}$ |
| 300 °C | $6.647 \times 10^{-5}$ | 0.455 | $1.04 \times 10^{-3}$ | $1.512 \times 10^{-12}$ | $2.603 \times 10^{-17}$ |
| 350 °C | $4.390 \times 10^{-5}$ | 1.512 | $2.58 \times 10^{-3}$ | $3.901 \times 10^{-12}$ | $2.573 \times 10^{-16}$ |

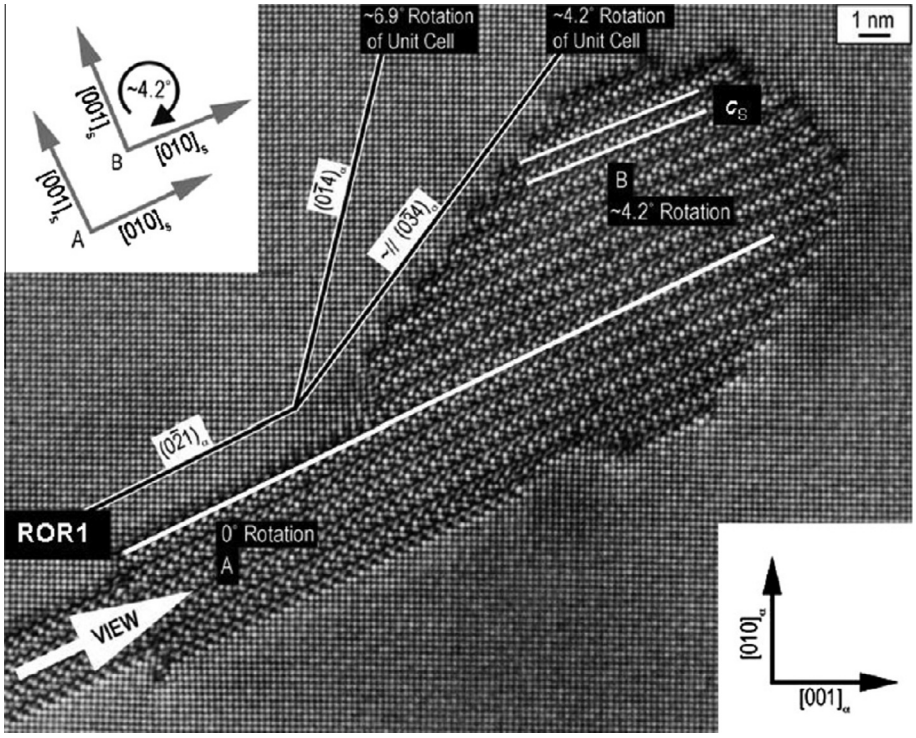


**Fig. 18.** An S phase particle observed by Winkelmann et al. [6] using high-resolution TEM, comprising two regions A and B that differ in orientation by a rotation of ~4.2°. These two domains could possibly correspond to the S1 and S2 phases observed in the present investigation, and if so, could lend support to the hypothesis that S2 nucleates on the S1/α-Al boundary, and absorbs solute *via* a moving interface.

## 6. Conclusions

In this investigation, the difference between the metastable and equilibrium S phases, S1 and S2, which form during the decomposition of Al—Cu—Mg solid solutions, has been determined using high-resolution synchrotron and neutron powder diffraction and atom probe tomography. Simultaneous Rietveld analysis of the synchrotron and neutron diffraction data has revealed no significant differences between the crystal structures of S1 and S2, however, both the powder diffraction and atom probe measurements indicate that the S1 phase forms with a slight deficiency in Cu. The atom probe results have also shown that GPB zones coexist with the S1 and S2 phases in specimens aged to peak hardness.

The competition in formation between the S1 and S2 phases has been characterised in detail for the first time by *in situ* synchrotron powder diffraction. These isothermal aging experiments have shown that S1 forms very rapidly, reaching its maximum concentration in only a few minutes at high temperatures, whilst complete conversion to the S2 phase can take thousands of hours at low temperature. During aging, the unit cell volume of S1 increases, suggesting that vacancies on the Cu sites are gradually being filled. However, the S1 diffraction peaks remain distinct throughout the transformation, and do not just merge gradually into those of the S2 phase as the precipitates grow in size.

An analysis of the transformation kinetics using several different models has revealed that the S1 phase forms with an average activation energy of around 75 kJ/mol, which is much lower than the activation energies for Cu and Mg diffusion in an Al matrix (136 and 131 kJ/mol, respectively). Given that S1 and S2 have very similar compositions, and the total amount of S phase (S1 + S2) remains constant after the first few hours of aging, the transformation mechanism is thought to be a form of discontinuous coarsening, which may involve the nucleation of S2 precipitates at the S1/α-Al interface and the migration of an internal S1/S2 interface.

## Acknowledgments

This research was undertaken on the Powder Diffraction beamline at the Australian Synchrotron, Victoria, Australia (Experiments 5321 and 7230). Experiments at the ISIS Pulsed Neutron and Muon Source were supported by a beamtime allocation from the Science and Technology Facilities Council (Experiment RB1320197). The authors wish to thank beamline scientist Dr Aziz Daoud-Aladine for his assistance in setting up the HRPD instrument at ISIS, and

Dr Santiago Corujeira Gallo for assistance with the *in situ* synchrotron data collection. Atom probe tomography measurements were carried out with the support of the Deakin University Advanced Characterisation Facility.

MJS and MAG acknowledge the support of CSIRO through the Office of the Chief Executive (OCE) Science Program. TJB gratefully acknowledges the support of CSIRO's OCE Science Leader program and the Advanced Materials transformational capability platform for this work.

## References

[1] H. Perlitz, A. Westgren, The crystal structure of $Al_2CuMg$, Ark. Kemi Mineral. Geol. B16 (1943) 1–5.
[2] V. Radmilovic, R. Kilaas, U. Dahmen, G.J. Shiflet, Structure and morphology of S-phase precipitates in aluminum, Acta Mater. 47 (1999) 3987–3997.
[3] A.K. Gupta, P. Gaunt, M.C. Chaturvedi, The Crystallography and Morphology of the S'-Phase Precipitate in an Al(CuMg) Alloy, Philos. Mag. Phys. Condens. Matter Struct. Defects Mech. Prop. 55 (1987) 375–387.
[4] C.B. Zhang, W. Sun, H.Q. Ye, Investigation of the crystallography and morphology of the S′ precipitate in an Al(CuMg) alloy by HREM, Philos. Mag. Lett. 59 (1989) 265–271.
[5] J. Majimel, G. Molenat, F. Danoix, O. Thuillier, D. Blavette, G. Lapasset, et al., High-resolution transmission electron microscopy and tomographic atom probe studies of the hardening precipitation in an Al–Cu–Mg alloy, Philos. Mag. 84 (2004) 3263–3280.
[6] G.B. Winkelman, K. Raviprasad, B.C. Muddle, Orientation relationships and lattice matching for the S phase in Al–Cu–Mg alloys, Acta Mater. 55 (2007) 3213–3228.
[7] S.C. Wang, M.J. Starink, Two types of S phase precipitates in Al–Cu–Mg alloys, Acta Mater. 55 (2007) 933–941.
[8] M.J. Styles, C.R. Hutchinson, Y. Chen, A. Deschamps, T.J. Bastow, The coexistence of two S ($Al_2CuMg$) phases in Al–Cu–Mg alloys, Acta Mater. 60 (2012) 6940–6951.
[9] Y.A. Bagaryatsky, Dokl. Akad. Nauk SSSR. 87 (1952) 397.
[10] Y.A. Bagaryatsky, Dokl. Akad. SSSR 87 (1952) 559–562.
[11] J.M. Silcock, The structural ageing characteristics of Al–Cu–Mg alloys with copper: magnesium weight ratios of 7: 1 and 2.2: 1, J. Inst. Met. 89 (1961) 203–210.
[12] L. Kovarik, S.A. Court, H.L. Fraser, M.J. Mills, GPB zones and composite GPB/GPBII zones in Al–Cu–Mg alloys, Acta Mater. 56 (2008) 4804–4815.
[13] F. Cuisiat, P. Duval, R. Graf, Etude des premiers stades de decomposition d'un alliage Al–Cu–Mg, Scr. Metall. 18 (1984) 1051–1056.
[14] P. Ratchev, B. Verlinden, P. De Smet, P. Van Houtte, Precipitation hardening of an Al–4.2 wt% Mg–0.6 wt% Cu alloy, Acta Mater. 46 (1998) 3523–3533.
[15] A.M. Zahra, C.Y. Zahra, C. Alfonso, A. Charaï, Comments on "cluster hardening in an aged Al-Cu-Mg alloy", Scr. Mater. 39 (1998) 1553–1558.
[16] A. Charai, T. Walther, C. Alfonso, A.-M. Zahra, C.Y. Zahra, Coexistence of clusters, GPB zones, S″-, S′- and S-phases in an Al–0.9% Cu–1.4% Mg alloy, Acta Mater. 48 (2000) 2751–2764.
[17] S.C. Wang, M.J. Starink, The assessment of GPB2/S″ structures in Al–Cu–Mg alloys, Mater. Sci. Eng. A 386 (2004) 156–163.
[18] R.N. Wilson, P.G. Partridge, The nucleation and growth of S' precipitates in an aluminium-2.5% copper-1.2% magnesium alloy, Acta Metall. 13 (1965) 1321–1327.
[19] G.C. Weatherly, R.B. Nicholson, An electron microscope investigation of the interfacial structure of semi-coherent precipitates, Philos. Mag. 17 (1968) 801–831.
[20] S.P. Ringer, T. Sakurai, I.J. Polmear, Origins of hardening in aged Al–Cu–Mg–(Ag) alloys, Acta Mater. 45 (1997) 3731–3744.
[21] S.P. Ringer, S.K. Caraher, I.J. Polmear, Response to comments on cluster hardening in an aged Al–Cu–Mg alloy, Scr. Mater. 39 (1998) 1559–1567.
[22] S.C. Wang, M.J. Starink, Precipitates and intermetallic phases in precipitation hardening Al–Cu–Mg–(Li) based alloys, Int. Mater. Rev. 50 (2005) 193–215.
[23] L. Kovarik, M.K. Miller, S.A. Court, M.J. Mills, Origin of the modified orientation relationship for S(S″)-phase in Al–Mg–Cu alloys, Acta Mater. 54 (2006) 1731–1740.
[24] B. Heying, R. Hoffmann, R. Pottgen, Structure refinement of the S-phase precipitate $MgCuAl_2$, Z. Naturforsch. Sect. B J. Chem. Sci. 60 (2005) 491–494.
[25] A. Deschamps, T.J. Bastow, F. de Geuser, A.J. Hill, C.R. Hutchinson, In situ evaluation of the microstructure evolution during rapid hardening of an Al–2.5Cu–1.5Mg (wt.%) alloy, Acta Mater. 59 (2011) 2918–2927.
[26] K.D. Ralston, N. Birbilis, M. Weyland, C.R. Hutchinson, The effect of precipitate size on the yield strength-pitting corrosion correlation in Al–Cu–Mg alloys, Acta Mater. 58 (2010) 5941–5948.
[27] ThermoCalc, n.d.
[28] B. Gault, M.P. Moody, J.M. Cairney, S.P. Ringer, Atom Probe Microscopy, Springer, New York, 2012.
[29] B. Gault, M.P. Moody, F. de Geuser, G. Tsafnat, A.L. Fontaine, L.T. Stephenson, et al., Advances in the calibration of atom probe tomographic reconstruction, J. Appl. Phys. 105 (2009) 034913.
[30] M.P. Moody, B. Gault, L.T. Stephenson, D. Haley, S.P. Ringer, Qualification of the tomographic reconstruction in atom probe by advanced spatial distribution map techniques, Ultramicroscopy 109 (2009) 815–824.
[31] M.W. Johnson, W.I.F. David, HRPD: The High Resolution Powder Diffractometer at the SNS, Rutherford Appleton Laboratory, 1985.
[32] R.M. Ibberson, Design and performance of the new supermirror guide on HRPD at ISIS, Nucl. Instrum. Methods Phys. Res. Sect. A 600 (2009) 47–49.
[33] K.S. Wallwork, B.J. Kennedy, D. Wang, The high resolution powder diffraction beamline for the Australian synchrotron, in: J. Choi, S. Rah (Eds.), AIP Conf. Proc., American Inst Physics, Melville, 2007, pp. 879–882.
[34] H.P. Klug, L.E. Alexander, X-ray Diffraction Procedures for Polycrystalline and Amorphous Materials, second ed., Wiley, New York, 1974.
[35] M.R. Rowles, CONVAS2: a program for the merging of diffraction data, Powder Diffr. 25 (2010) 297–301.
[36] H.M. Rietveld, A profile refinement method for nuclear and magnetic structures, J. Appl. Crystallogr. 2 (1969) 65–71.
[37] R.A. Young, The Rietveld method, International Union of Crystallograhy, Oxford University Press, Chester, England, Oxford, New York, 1993.
[38] R.J. Hill, I.C. Madsen, The effect of profile-step counting time on the determination of crystal structure parameters by X-ray Rietveld analysis, J. Appl. Crystallogr. 17 (1984) 297–306.
[39] W.A. Dollase, Correction of intensities for preferred orientation in powder diffractometry: application of the March model, J. Appl. Crystallogr. 19 (1986) 267–272.
[40] N.C. Popa, D. Balzar, Size-broadening anisotropy in whole powder pattern fitting. Application to zinc oxide and interpretation of the apparent crystallites in terms of physical models, J. Appl. Crystallogr. 41 (41) (2008) 615–627.
[41] R.K.W. Marceau, G. Sha, R.N. Lumley, S.P. Ringer, Evolution of solute clustering in Al–Cu–Mg alloys during secondary ageing, Acta Mater. 58 (2010) 1795–1805.
[42] G. Sha, R.K.W. Marceau, X. Gao, B.C. Muddle, S.P. Ringer, Nanostructure of aluminium alloy 2024: segregation, clustering and precipitation processes, Acta Mater. 59 (2011) 1659–1670.
[43] R.J. Hill, C.J. Howard, Quantitative phase analysis from neutron powder diffraction data using the Rietveld method, J. Appl. Crystallogr. 20 (1987) 467–474.
[44] J. da Costa Teixeira, D.G. Cram, L. Bourgeois, T.J. Bastow, A.J. Hill, C.R. Hutchinson, On the strengthening response of aluminum alloys containing shear-resistant plate-shaped precipitates, Acta Mater. 56 (2008) 6109–6122.
[45] J. da Costa Teixeira, L. Bourgeois, C.W. Sinclair, C.R. Hutchinson, The effect of shear-resistant, plate-shaped precipitates on the work hardening of Al alloys: towards a prediction of the strength–elongation correlation, Acta Mater. 57 (2009) 6075–6089.
[46] C.R. Hutchinson, Modeling the kinetics of precipitation in aluminium alloys, in: R. Lumley (Ed.), Fundamentals of Aluminium Metallurgy, Woodhead Publishing, 2011, pp. 422–467.
[47] W.Z. Han, A. Vinogradov, C.R. Hutchinson, On the reversibility of dislocation slip during cyclic deformation of Al alloys containing shear-resistant particles, Acta Mater. 59 (2011) 3720–3736.
[48] Y. Chen, M. Weyland, C.R. Hutchinson, The effect of interrupted aging on the yield strength and uniform elongation of precipitation-hardened Al alloys, Acta Mater. 61 (2013) 5877–5894.
[49] W.A. Johnson, R.F. Mehl, Reaction kinetics in processes of nucleation and growth, Trans. Am. Inst. Min. Metall. Eng. 135 (1939) 416–442.
[50] M. Avrami, Kinetics of Phase Change. I General Theory, J. Chem. Phys. 7 (1939) 1103–1112.
[51] M. Avrami, Kinetics of phase change. II transformation-time relations for random distribution of nuclei, J. Chem. Phys. 8 (1940) 212–224.
[52] M. Avrami, Granulation, phase change, and microstructure kinetics of phase change. III, J. Chem. Phys. 9 (1941) 177–184.
[53] A.N. Kolmogorov, Zur statistik der kristallisationsvorgänge in metallen, Izv. Akad. Nauk SSSR Ser. Mat. 1 (1937) 355–359.
[54] F.S. Ham, Diffusion-limited growth of precipitate particles, J. Appl. Phys. 30 (1959) 1518–1525.
[55] M. Hillert, The kinetics of the first stage of tempering, Acta Metall. 7 (1959) 653–658.
[56] E.-S. Lee, Y.G. Kim, A transformation kinetic model and its application to Cu–Zn–Al shape memory alloys—I. Isothermal conditions, Acta Metall. Mater. 38 (1990) 1669–1676.
[57] F.L. Cumbrera, F. Sánchez-Bajo, The use of the JMAYK kinetic equation for the analysis of solid-state reactions: critical considerations and recent interpretations, Thermochim. Acta 266 (1995) 315–330.
[58] M.J. Starink, A.M. Zahra, An analysis method for nucleation and growth controlled reactions at constant heating rate, Thermochim. Acta 292 (1997) 159–168.
[59] J.W. Christian, The Theory of Transformations in Metals and Alloys, third ed., Pergamon, Amsterdam; Boston, 2002.
[60] M.J. Starink, On the meaning of the impingement parameter in kinetic equations for nucleation and growth reactions, J. Mater. Sci. 36 (2001) 4433–4441.
[61] M.J. Starink, Kinetic equations for diffusion-controlled precipitation reactions, J. Mater. Sci. 32 (1997) 4061–4070.
[62] M.J. Starink, A.-M. Zahra, Mechanisms of combined GP zone and θ′ precipitation in an Al–Cu alloy, J. Mater. Sci. Lett. 16 (1997) 1613–1615.
[63] M.J. Starink, A.-M. Zahra, β′ and β precipitation in an Al–Mg alloy studied by DSC and TEM, Acta Mater. 46 (1998) 3381–3397.

[64] M.J. Starink, P. Wang, I. Sinclair, P.J. Gregson, Microstrucure and strengthening of Al–Li–Cu–Mg alloys and MMCs: I. Analysis and modelling of microstructural changes, Acta Mater. 47 (1999) 3841–3853.
[65] J.B. Austin, R.L. Rickett, Kinetics of the decomposition of austenite at constant temperature, Trans. Am. Inst. Min. Metall. Eng. 135 (1939) 396–415.
[66] M.V. Speight, Growth kinetics of grain-boundary precipitates, Acta Metall. 16 (1968) 133–135.
[67] J.J. Hoyt, On the coarsening of precipitates located on grain boundaries and dislocations, Acta Metall. Mater. 39 (1991) 2091–2098.
[68] A.J. Ardell, Interfacial free energies and solute diffusivities from data on Ostwald ripening, Interface Sci. 3 (1995) 119–125.
[69] E. Kozeschnik, Modeling Solid-state Precipitation, Momentum Press, New York, 2013.
[70] W.D. Callister, Materials Science and Engineering: An Introduction, sixth ed., John Wiley & Sons, New York, NY, 2003.
[71] M. Hillert, Jernkont. Ann. 141 (1957) 757–789.
[72] J.E. Hatch (Ed.), Aluminum: Properties and Physical Metallurgy, American Society for Metals, Metals Park, Ohio, 1984.
[73] T.J. Bastow, 63Cu NMR analysis of microstructure evolution in Al–Cu–Mg alloys, Philos. Mag. 85 (2005) 1053–1066.
[74] T.J. Bastow, A.J. Hill, Early stage hardening in AlCuMg alloy studied by 63Cu nuclear magnetic resonance and positron annihilation, Mater. Sci. Forum. 519–521 (2006) 1355–1360.
[75] R.K.W. Marceau, G. Sha, R. Ferragut, A. Dupasquier, S.P. Ringer, Solute clustering in Al–Cu–Mg alloys during the early stages of elevated temperature ageing, Acta Mater. 58 (2010) 4923–4939.
[76] B. Klobes, K. Maier, T.E.M. Staab, Natural ageing of Al–Cu–Mg revisited from a local perspective, Mater. Sci. Eng. A 528 (2011) 3253–3260.